UNUSUAL FUNCTIONALITIES IN SHAPE MEMORY ALLOYS

A Dissertation

by

JAMES ALAN MONROE

Submitted to the Office of Graduate Studies of
Texas A&M University
in partial fulfillment of the requirements for the degree of

DOCTOR OF PHILOSOPHY

Chair of Committee,   Ibrahim Karaman
Committee Members,   Raymundo Arroyave
                                  Karl T. Hartwig
                                  Dimitris Lagoudas
Head of Department,   Andreas A. Polycarpou

August 2013

Major Subject: Mechanical Engineering

ABSTRACT

Shape memory alloys have received extensive attention in the past 40 years for their superelastic and actuator capabilities, but their application potential is much greater than these two fields. In this work, we explore unique processing routes that lead to new functionalities, such as tissue scaffolds; magneto/elasto caloric; magnetic sensing; perfect one-way actuation and tailored thermal expansion coefficients, in materials that undergo martensitic transformation.

First, we show that NiMn based metamagnetic shape memory alloys can be processed into foams with a selected pore size using solid state replication. This enhances the material's mechanical and heat transfer properties which make it attractive for biomedical implants and magneto/elasto caloric applications. We also explore the biocompatibility of these NiMn based alloys. While the base alloys are shown to be cytotoxic, a layer-by-layer assembled polymer passivation layer is used to improve the biocompatibility.

Next, we examine two unique types of glass in NiMn based shape memory alloys that can be stabilized with simple secondary heat treatments. Generalized glassy theory has been used to describe rotational/translational frustration of symmetry in many material systems and functional domains. This theory is extended to the strain domain of thermoelestic transitions to explain frustration observed in the diffusionless martensitic transformations. We show that this "strain glass" frustration can be created through secondary heat treatments on a single magnetic shape memory alloy composition and

link the responsible defect structures to cluster spin glass transitions and an experimentally measured Kauzmann point. These results show the power of glassy theory to extend beyond the currently known functional domains and can potentially extend shape memory alloys into magnetic sensing and perfect one-way actuation applications.

Last, we propose a statistical thermodynamic model to explain the huge thermal expansion anisotropy exhibited by many martensitic alloys. We show that this model can be used to predict thermal expansion anisotropy directions in many martensitic alloy systems. Processing is then used to tailor the macroscopic thermal expansion coefficient for a NiTiPd test material. This provides scientists and engineers with a previously unavailable design tool which can fulfill the need for thermal expansion compensation.

DEDICATION

To my family, for their support, encouragement and patience.

ACKNOWLEDGEMENTS

Firstly, I want to acknowledge Dr. Ibrahim Karaman, my adviser and mentor, who has guided me from the beginning of my scientific career. Although I started cutting samples in the machine shop as a student worker, the laboratory environment he fostered allowed me to grow in knowledge and capacity. The large number of opportunities for international research and collaboration he provided has given me unique perspectives on materials science and engineering. The freedom to explore research topics that interest me has been invaluable to helping me become a more independent researcher. My achievements towards this degree would not have been possible without him.

I also acknowledge my committee members, Dr. Raymundo Arroyave; Dr. Ted Hartwig and Dr. Dimitris Lagoudas. I have had the privilege of attending classes taught by each of these professors and learned a great deal from each of them. I want to specifically thank Dr. Arroyave for his open door policy and always fascinating conversations about materials science and thermodynamics, Dr. Hartwig for his mentorship when teaching my first class and Dr. Lagoudas for his support of international collaboration and his unrelenting attention to detail which forces students to think critically.

Next I want to thank the current and past members of my research lab. From the beginning Ersin Karaca, Burak Bassaran, Benat Kockar, Andrew (Andy) Brewer and Mohammed Haouaoui tolerated my constant questions and gave me the foundations for hands on experimental research. Thanks also to Nick Barta, Nick Bruno, Alper Evirgen, Ebubekir Dogan, Ankush Kothalkar, Liangfa Hu, Ceylan Hayrettin, Li-Wei Tseng, Brian

NOMENCLATURE

A	Austenite
Å	Angstrom
a_{ij}	Lattice Spacing Matrix
A_f	Austenite Finish
APB	Anti Phase Boundary
A_s	Austenite Start
BCC	Body Centered Cubic
B2	Ordered Body Centered Cubic
ºC	Degrees Celcius
CC	Clausius Clapeyron
CsCl	Cesium Chloride Structure (B2)
CR	Cold Rolling
CTE	Coefficient of Thermal Expansion
CW	Cold Work
DMA	Dynamic Mechanical Analysis
DF	Dark Field
E_a	Activation Energy
ED	Extrusion Direction
EDM	Electro-Discharge Machining
emu	Electromagnetic Units

E'	Real Part of Dynamic Elastic Modulus
FC	Field Cooled
G	Gibb's Free Energy
g	Gram
GSAS	General Structure Analysis System
H	Magnetic Field
K	Kelvin
k_B	Boltzmann Constant
LANSCE	Los Alamos Neutron Science Center
$L2_1$	Heusler Crystal Structure
M	Magnetization
M'	Real Part of AC Magnetization
M_f	Martensite Finish
MFIPT	Magnetic Field Induced Phase Transformation
MFIS	Magnetic Field Induced Strain
Micro-MTM	Micro Magneto-Thermo-Mechanical Test Frame
micro-CT	X-Ray Microtomography
MMSMA	Meta-Magnetic Shape Memory Alloy
MPa	Mega Pascal
M_s	Martensite Start
MSMA	Magnetic Shape Memory Alloy
ND	Normal Direction

NTE	Negative Thermal Expansion
P	Pressure
PAA	Poly [Acrylic Acid]
PAH	Poly [Allylamine Hydrochloride]
PEGDA	Poly [Ethylene Glycol] Diacrylate
PTE	Positive Thermal Expansion
R	Ideal Gas Constant
RD	Rolling Direction
RKKY	Ruderman-Kittel-Kasuya-Yosida
S	Entropy
SAM	Self Accomodated Martensite
SEM	Scanning Electron Microscopy
SMA	Shape Memory Alloy
SMARTS	Spectrometer for Materials Research at Temperature and Stress
SOM	Stress Oriented Martensite
SQUID	Superconducting Quantum Interference Device
T	Temperature (Thermal Context)
T	Tesla (Magnetic Field Unit Context)
T_C	Currie Temperature
TD	Transverse Direction
TEM	Transmission Electron Microscopy
T_f	Cluster Spin Glass Freezing Temperature

T_g	Glass Transition Temperature
T_K	Kauzmann Temperature
TMA	Thermomechanical Analyzer
TOF	Time of Flight
TTT	Transformation-Temperature-Time
UHP	Ultra High Purity
V	Volume
VSM	Vibrating SQUID Module
WQ	Water Quench
X-Link	Crosslink
XRD	X-Ray Diffraction
ZFC	Zero Field Cooled
α	Isotropic Thermal Expansion
ϵ_{ij}	Thermal Expansion Tensor
τ	Relaxation Time

TABLE OF CONTENTS

LIST OF FIGURES

xiii

LIST OF TABLES

CHAPTER I

INTRODUCTION

1.1 Motivation

Shape memory and meta-magnetic shape memory alloys are most studied for their ability to link magnetic, thermal and mechanical energy domains via a first order martensitic phase transformation. More recently, glassiness in the first order phase transformation and giant positive and negative thermal expansion in the martensitic phases of these alloy systems has been observed. While these unique properties show great promise for unique applications, such as solid state actuators; sensing devices; energy harvesters; magnetic and elastic refrigeration; perfect one way actuation and thermal expansion compensation, they are in limited industrial use due to brittleness, large hysteretic behavior (magnetic and thermal), slow thermal response time and lack of information on the glassy and thermal expansion characteristics. The three specific aims of this work, 1) Magnetically morphing tissue scaffolds; 2) Glassiness in shape memory alloys and 3) Thermal expansion properties in martensitic alloys, are designed to expand the utility of traditional and magnetic shape memory alloys by via processing and exploring their unique properties for innovative applications.

1.2 Magnetically Morphing Tissue Scaffolds

The first of these specific aims explores the creation of MMSMA foam actuators using solid state replication for use as magnetically morphing tissue scaffolds. NiCoMnSn has been selected for this study because it is easily sintered and shows

magnetic field induced phase transformation [1]. Consolidation through spark plasma sintering of powders has been shown to increase the toughness in polycrystalline NiCoMnSn [1]. Pressureless sintering has also been used to produce NiCoMnSn foams with pores ~10µm [1,2]. Increasing the porosity by varying the sintering time was shown to decrease toughness while increasing strain recovery by heating after compressive deformation. While the results in [2] are promising, introducing a selected pore size, volume fraction and distribution is vital for further improving and tailoring the material's properties for specific applications. Solid state replication has been used in NiMnGa magnetic shape memory alloys [3,4] and NiCoMnIn MMSMAs [5]. Solid state replication from co-compaction of space holder and alloy powders was selected for this study because it allows accurate selection of pore size, pore distribution and relative density. Introducing interconnected pores of a select size can allow tissue ingrowth for biomedical applications and faster heat transfer during the first order transformation via convection. An increased heat transfer rate can potentially allow the use of these alloys in a wide range of applications where fast frequency response is required; such as wireless micropumps and efficient magnetic refrigerators. While porous NiCoMnIn MMSMAs have been fabricated using solid state replication oxygen contamination from the powder metallurgy approach prevented the martensitic transformation [5]. This current work utilizes solid state replication to create the first ever MMSMA foam with a selected pore size that shows MFIPT. Magneto-thermal, thermo-mechanical and cytotoxicity data is presented and future work on augmenting the mechanical response is discussed.

1.3 Glassiness in Shape Memory Alloys

The second specific aim determines the role of glassiness, both strain and cluster-spin, and changes in autensite's and martensite's relative entropy, known as a Kauzmann Paradox, on the arrest of the martensitic transformation in NiCoMnIn MMSMAs. Glassiness and relaxation has been attributed to disorder and defects in these ordered systems, but the identity of these defects has not been determined. Strain glassiness has been directly observed in Ni-rich NiTi SMAs and is attributed the large number of defects present in the material that cause a frustration of the austenite to martensite transformation [6]. Indications of a strain glass and relaxation phenomena have been observed in NiMnX based MMSMAs and is dependent upon the B2 to L2$_1$ ordering, but there has been no direct observation of a glass transition [7]. While the spin-glass freezing of the martensitic phase has been observed and explored [8], there is no research on the effect of ordering on the spin-glass freezing point. The higher ordering in these materials presents a unique opportunity to help determine the defect structures responsible for the glassiness observed SMAs. The role of disorder on the entropy difference between austenite and martensite has not been explored either. Direct observation of a Kauzmann point and cluster-spin glass freezing is presented while future work will focus on the direct observation of the strain glass freezing point and beginning to determine the defect structures responsible for these phenomena.

1.4 Thermal Expansion Properties in Martensitic Alloys

The third specific aim looks to the martensitic phase and not the martensitic transformation of SMAs to determine their potential as negative and zero thermal

expansion materials. The only published research focusing on the unusual thermal expansion properties martensitic NiTi showed that the thermal expansion response is highly anisotropic with contraction in one crystallographic direction and expansion in the others [9]. Negative thermal expansion has also been observed in thermo-mechanical experiments on polycrystalline NiTiPd [10], but little attention to has been paid to its practical applications. Unpublished work with our collaborators shows giant positive thermal expansion (PTE) and negative thermal expansion (NTE) in NiMnGa. We propose a statistical thermodynamic model for predicting PTE and NTE directions in shape memory alloys and show that simple processing routes can produce macroscopic tailored thermal expansion coefficients.

1.5 The Thermodynamics of Shape Memory Alloys

Shape memory alloys (SMAs) are transducers that change one form of energy into another via a reversible first order phase transformation. Traditional SMAs can only link thermal and mechanical energy while magnetic and meta-magnetic SMAs can link thermal, mechanical and magnetic energy domains. As such, the energy link between these domains can be described using traditional thermodynamic equations of state. In this section, a general energy potential to link these three domains is developed and a thermodynamic relationship between the high symmetry austenite and low symmetry martensite phases is derived using the Clausius Clapeyron relationship. These general relationships are used throughout the rest of the manuscript.

Firstly, we assume the internal energy of a system, U, is a function of the relevant extensive variables and equals the energy put into the system minus the energy taken out.

$$U = f(S, V, M, \varepsilon) = energy\ in - energy\ out$$

Here S is entropy, V is volume, M is magnetization and ε is strain which correspond to displacements in the thermal, hydrostatic mechanical, magnetic and directional mechanical energy domains, respectively. Taking the sign convention where magnetic and thermal energy is put into the system and mechanical energy is work done by the system we obtain a differential form of the internal energy which is the sum of respective energy terms.

$$dU = TdS + HdM - V\sigma d\varepsilon - PdV$$

Here H is magnetic field, T is temperature, σ is stress and P is pressure that all correspond to intensive variables imposed on the system by their respective energy domains. Figure 1 graphically displays the relevant energy domains and shows that integration of the equation above would result in the summation of the areas under each of the corresponding curves. This area represents the energy contributions from varying the extensive variables while measuring the intensive variables.

Unfortunately, using entropy, magnetization, strain and volume as control variables is experimentally difficult if not impossible in some cases. Therefore, using the complementary energy function which is a function of intensive variables is invaluable for designing experiments and analyzing data. A general free energy function is proposed as:

5

$$\Psi = U - TS - HM + V\sigma\varepsilon + PV$$

where Ψ is the free energy function and the rest of the terms are as defined above. By combining this equation with the differential form stated above we obtain:

$$d\Psi = -SdT - MdH + V\varepsilon d\sigma + VdP$$

This form uses the complementary energy in each energy domain where integration results in the area to the left of each of the curves displayed in Figure 1. This equation is applied to each phase independently to obtain the free energy of that particular phase. Controlling the intensive variables and measuring the extensive variables of the system is experimentally advantageous for determining the equilibrium conditions between two competing phases.
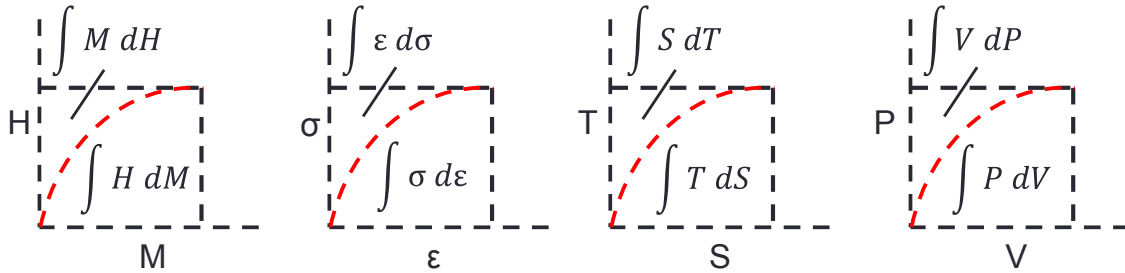
Figure 1. Graphical representations of intensive variables (magnetic field H, stress σ, temperature T and pressure P) vs. extensive variables (magnetization M, strain ε, entropy S and volume V) showing the displacement and complementary energy contributions for each energy domain.

Next, we will use the Clausius Clapeyron (CC) relationship and the energy potential developed above to determine the phase equilibrium conditions between the austenite and martensite phases. It is first assumed that there is a condition where

coexistence of the two phases occurs. When this is realized at equilibrium conditions, it is assumed that the intensive variables and the free energy for both phases are equal to one another:

$$dT^A = dT^M; \quad dH^A = dH^M; \quad d\sigma^A = d\sigma^M; \quad dP^A = dP^M; \quad d\Psi^A = d\Psi^M$$

where A and M correspond to the austenite and martensite phases, respectively. By taking the free energies of the two phases to be equal to one another and $\Delta X^{A \to M} = X^M - X^A$ we obtain:

$$-S^A dT - M^A dH + V^A \varepsilon^A d\sigma + V^A dP = -S^M dT - M^M dH + V^M \varepsilon^M d\sigma + V^M dP$$

$$\Delta S^{A \to M} dT = -\Delta M^{A \to M} dH + V \Delta \varepsilon^{A \to M} d\sigma + \Delta V^{A \to M} dP$$

This general form of the CC relationship is used to determine which variable to hold constant, which to vary and which to measure to experimentally determine the equilibrium between the austenite and martensite phases. Table 1 displays the six possible CC relationships described by the above equation. Since pressure is held constant for all experiments subsequently shown, we can safely ignore this term as dP is zero. We can clearly see that the extensive variables are measured while the intensive variables are either constant, held at various discrete values or ramped. This results from the use of a free energy function that relies on the complementary energy. It should also be noted that with the exclusion of the magnetic energy domain for traditional shape memory alloys, the first two relationships still hold and are the ones commonly used in the evaluation of all shape memory alloy systems.

Table 1. The six independent Clausius Clapeyron (CC) relationships, the discrete; ramped or constant intensive variables and the measured extensive variables.

CC Equation	T	S	H	M	σ	ε
$\dfrac{d\sigma}{dT} = \dfrac{\Delta S^{A\to M}}{V\Delta\varepsilon^{A\to M}}$	Various Discrete	-	Constant	Measure	Ramp	Measure
$\dfrac{dT}{d\sigma} = \dfrac{V\Delta\varepsilon^{A\to M}}{\Delta S^{A\to M}}$	Ramp	-	Constant	Measure	Various Discrete	Measure
$\dfrac{dH}{dT} = \dfrac{-\Delta S^{A\to M}}{\Delta M^{A\to M}}$	Various Discrete	-	Ramp	Measure	Constant	Measure
$\dfrac{dT}{dH} = \dfrac{-\Delta M^{A\to M}}{\Delta S^{A\to M}}$	Ramp	-	Various Discrete	Measure	Constant	-
$\dfrac{d\sigma}{dH} = \dfrac{\Delta M^{A\to M}}{V\Delta\varepsilon^{A\to M}}$	Constant	-	Various Discrete	Measure	Ramp	Measure
$\dfrac{dH}{d\sigma} = \dfrac{V\Delta\varepsilon^{A\to M}}{\Delta M^{A\to M}}$	Constant	-	Ramp	Measure	Various Discrete	Measure

CHAPTER II

MAGNETICALLY MORPHING TISSUE SCAFFOLDS[*]

2.1 Introduction

Morphing tissue scaffolds provide support for cellular growth much like a structural scaffold provides support for a building and can "massage" bodily tissues which has been shown to stimulate bone cell growth [11,12]. Magnetic shape memory alloys (MSMAs) are metallic materials that link magnetic, thermal and mechanical energy domains; in other words they can convert one form of energy into another. While these properties show great promise for unique biomedical applications such as morphing tissue scaffolds and micro-pumps that can be activated from outside the body using magnetic fields, current MMSMAs are very brittle and their actuation frequency is very low [13]. Inter-granular brittleness is an issue in NiMn based MMSMAs due to the limited number of deformation slip systems for accommodating deformations in the cubic austenite to tetragonal martensitic transformation [13]. Previous research on NiCoMnSn, Figure 2, and NiMnGa has showed that introducing pores into the material can improve the ductility and actuation frequency [1,14]. Also, bone tissue scaffolds require interconnected pore sizes on the order of 500 microns to bond to bodily tissue and allow the transport of nutrients and waste. This current area of research shows that a powder metallurgy approach can be used to fabricate MMSMA alloy foams with large 500

[*] Sections reprinted with permission from Monroe, J. A. *et al.* Magnetic response of porous NiCoMnSn metamagnetic shape memory alloys fabricated using solid-state replication. *Scripta Materialia* **67**, (2012). Copyright (2012) Elsevier.

micron interconnected pores. In addition to biomedical applications, the introduction of pores can help increase the heat transfer rate by increasing the surface area and allowing fluid flow through the material. This allows their utility in higher frequency applications and allows improved magneto and elasto-caloric effects for solid state refrigeration technology.
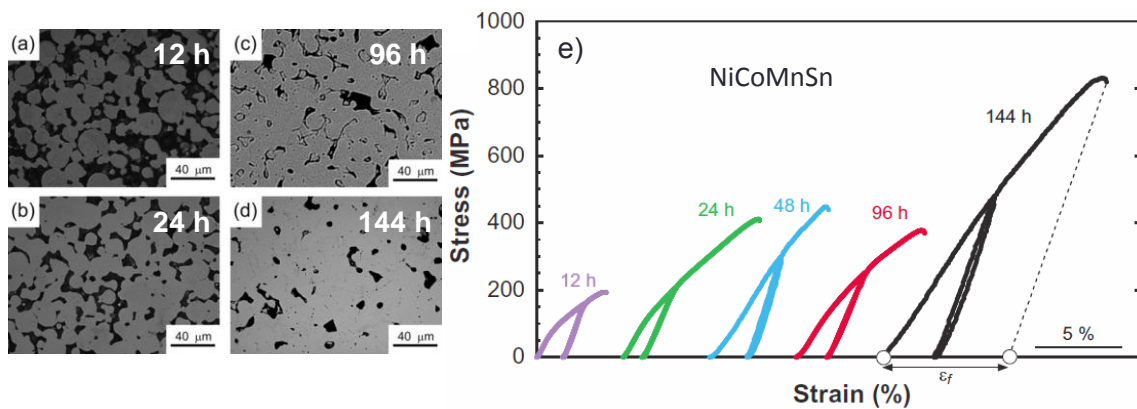
Figure 2. Optical micrographs showing pore morphology after a) 12 hour, b) 24 hour, c) 96 hour and d) 144 hour heat treatments and e) the stress-strain response showing increased heat treatment times increase fracture strength of the porous NiCoMnIn.

NiMnGa magnetic shape memory alloys (MSMAs) have received increasing attention in recent years for actuator applications due to their ability to undergo magnetic-field-induced martensite variant reorientation. However, they are prone to intergranular fracture in bulk polycrystalline form [13]. Previous research on NiMnGa MSMAs has shown that hot isostatic pressing can be used to create metallic foams with a selected pore size distribution [13]. The resulting foam material is not as prone to intergranular fracture and shows magnetic-field-induced martensite variant reorientation

with strains comparable to single crystalline NiMnGa MSMAs [13-15]. Introducing pores has also been shown to enhance the magnetocaloric effect by relaxing grain boundary constraints [16]. Unfortunately, MSMA actuation stresses are limited to <10 MPa in the bulk single crystalline form and this translates to low effective stresses MSMA foams can apply. These low actuation stresses are directly related to the limited amount of magneto-crystalline anisotropy energy available for rotating martensite variants [17].

Comparatively, metamagnetic SMAs (MMSMAs), such as NiCoMnX (X = Ga, In, Sn, Sb, Al), undergo magnetic-field-induced phase transformation (MFIPT) from a ferromagnetic austenite to a paramagnetic/antiferromagnetic martensite. The magnetic energy that can be converted into mechanical work originates from the difference in magnetic saturation levels between the two phases and is only limited by this difference and the magnitude of the applied magnetic field. This first order phase transformation can allow for actuation stresses of >100 MPa [17], but these alloys are prone to intergranular fracture much like NiMnGa. Consolidation through spark plasma sintering of powders has been shown to increase the toughness in polycrystalline NiCoMnSn [18]. Pressureless sintering has also been used to produce NiCoMnSn porous samples with pore sizes around 10 μm [1,2]. Increasing the porosity by varying the sintering time was shown to decrease toughness while increasing strain recovery by heating after compressive deformation. While the results in Ref. [2] are promising, introducing a selected pore size, volume fraction and distribution is vital for further improving and tailoring the material's properties. Solid-state replication from co-compaction of space holder and alloy powders was selected for this study because it has previously allowed

accurate selection of pore size, pore distribution and relative density in NiMnGa MSMAs [13-15] and NiCoMnIn MMSMAs [19].

Introducing interconnected pores of a select size can also allow faster heat transfer via convection during the first-order transformation and cell migration. An increased heat transfer rate can potentially allow the use of these alloys in a wide range of applications where a fast frequency response is required, such as wireless micropumps and efficient magnetic refrigerators. While porous NiCoMnIn MMSMAs have been fabricated using solid-state replication, no work was conducted on the material's magnetic, mechanical or thermal properties [19]. The current work utilizes solid-state replication to create the first MMSMA foam with a selected pore size that shows MFIPT.

The goal of this study is to create the first MMSMA foams with excellent magneto-thermo-mechanical coupling for biomedical applications. NiCoMnSn is selected for this study because its transformation temperatures are around body temperature and has been shown to sinter easily. The effect of solid state replication and strut density on the magneto-thermo-mechanical response of the material is examined while future work will focus on the effect of the macro-pore volume fraction.

The cytocompatibility of NiMnX alloys must be tested in order to further evaluate their potential for biomedical applications. This is particularly the case as previous in vitro testing has shown NiMnGa to be cytotoxic [20,21], and a range of studies have demonstrated the toxicity of both Ni [22-26] and Mn [27,28]. In the present study, we therefore examined the cytotoxicity of the NiMnSn member of the broader NiMnX (X =

Al, In, Sn and Sb) MSMA family. Sn was selected over In and Sb as the tertiary alloy component due to the high cytotoxicity of In and Sb relative to Mn, Ni, and Sn [29].

Passivation layers are also examined to prevent the corrosion and ion release of these alloys. PAH/PAA coatings were selected because they have been shown to significantly improve the corrosion resistance of aluminum [30] and reduce the transport of multivalent ions [31]. PAH/PAA coatings have also been shown to withstand the large cyclic deformation of SMA substrates [32,33] which would be experienced in an actuator application.

2.2 Experimental Methods

$Ni_{43}Co_7Mn_{39}Sn_{11}$ pre-alloyed powders were fabricated using gas atomization, then sieved to between 27 and 63 μm. This alloy composition was selected for its high Curie temperature, room-temperature martensitic transformation and ease of sintering [2,34]. Figure 3a displays magnetization results from the as-atomized and homogenized particles showing the need for homogenization at 900ºC for 24 hours. The scanning electron microscope (SEM) images displayed in Figure 3b and 3c show the inhomogeneous dendritic structure that remained from the atomization process. While 900ºC is sufficient to obtain a goo magneto-thermo response, the sintering was not sufficient to obtain good thermo-mechanical results as the samples crumbled after processing. Therefore, it was necessary to conduct a systematic factorial experiment to determine the most effective processing route for improved powder densification. Samples were compacted to various pressures and subjected to homogenization heat treatments at various times. Table 2 displays the resulting porosity for powders sintered

13

at various times, temperatures and initial compact pressures. It is evident that temperature and initial compact pressure have the greatest impact on densification.
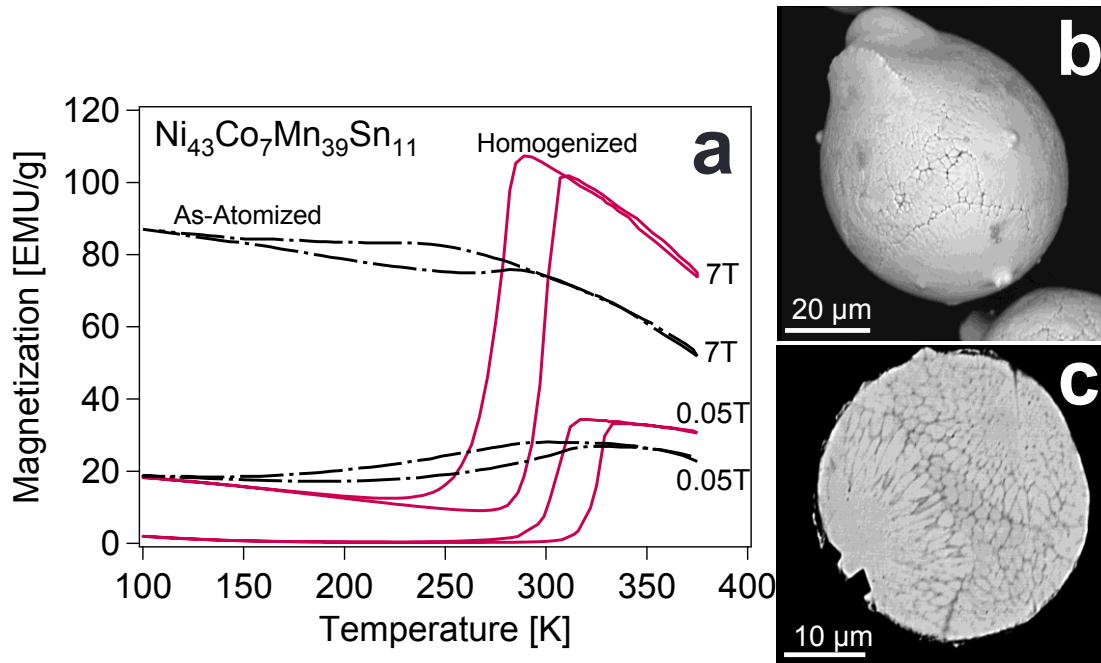
Figure 3. a) Magnetization measurements showing the response for the as-atomized and homogenized samples and b) secondary electron and c) backscatter electron scanning electron microscope images showing the inhomogeneity of the as-atomized particles.

Table 2. The resulting strut porosity from fractional factorial experiments.

Porosity [%]	Time [hr]	Temperature [K]	Compact Pressure [Mpa]
34.26	24	1173	200
29.22	24	1273	200
18.23	24	1323	200
26.4	12	1323	200
15.96	48	1323	200
15.58	12	1323	800

14

The specimens with a selected pore size were fabricated by blending the as-sieved powders and ammonium bicarbonate space holders with a particle size distribution between 350 and 500 μm. A volume fraction of 50% space holder was used for a target of 50% of 300 μm to 500 μm interconnected pores. Ammonium bicarbonate was selected as a space holder because it decomposes between 450 and 475 K, and can be removed during the sintering heat treatment [35]. A 2% aqueous solution, by mass, of polyvinyl alcohol binder was mixed with the powders to improve the green body strength. The powders were then placed in a 12.5 mm diameter die and cold pressed under 200 MPa in an environmental glove box. Flowing ultra-high-purity (UHP) argon over the specimens during the sintering process displaced oxygen and removed the burned binder and space holder from the environment. Oxygen contamination issues were solved by placing titanium getter in the furnace to scavenge oxygen during sintering. The heat treatments began with a temperature ramp at 5 K min^{-1} from room temperature to the desired sintering temperature, which was followed by a sustained hold at high temperature. This slow heating rate allows the space holder and binder to burn out before the sintering temperature is reached. Cooling was performed by moving the specimens to a water cooled area of the tube furnace held at 333 K for cooling under UHP argon.

Optical microscopy was performed to observe the powder sintering necks while X-ray micro-computed tomography (micro-CT) was performed on the porous sample to investigate the three-dimensional (3-D) representation of the large pore size distribution and interconnectivity. Point counting and thresholding techniques were used to

determine the porosity content from optical and micro-CT images, respectively, and good agreement was found. Figure 4 depicts an alloy foam with 50% large pore porosity using optical microscopy, a) and b), and micro-CT, c).
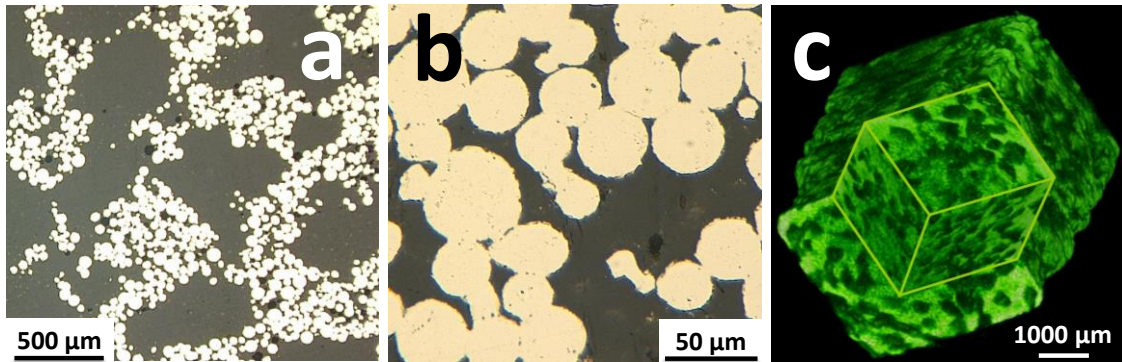
Figure 4. Optical microscopy, a) and b), and micro computer aided tomography (micro-CT) of a sample fabricated using ammonium bicarbonate as a space holder.

While these pre-alloyed powders have been shown to homogenize and sinter easily at 1173 K [1], the use of an oxygen getter suppressed the sintering process and required a systematic study of the effect of pre-compact pressure, sintering time and sintering temperature on the densification of the alloy. These three parameters were varied in a factorial design of experiments to determine the most effective parameters that enhance the sintering process.

The magneto-thermo coupling response was evaluated using a SQUID-VSM magnetometer that can apply 7T magnetic fields across a temperature range from 2.8 K to 400 K. Thermal cycles under constant magnetic field and isothermal magnetization

tests were conducted to characterize the magnetic properties and martensitic transformation characteristics of the material in different processing conditions.

Thermo-mechanical experiments to determine the shape memory properties and compressive fracture strength were conducted on a screw driven MTS system. Cooling was achieved by flowing liquid nitrogen through copper tubes wound around the compression grips while heating was achieved with resistance heating bands wrapped around the copper windings. Displacement was measured by placing the ceramic rods of an MTS high temperature extensometer on the grips directly above and below the sample.

NiMnSn samples were cut from a pre-alloyed and cast ingot into 10x10x1 mm^3 specimens and homogenized at 900ºC for 24 hours under argon in a sealed quartz ampule. For positive controls, 99.9% pure Sn and commercially pure grade 2 Ti were cut into 10x10x1 mm^3 samples and polished in the same manner. A diamond saw was used to cut 10x10x1 mm3 specimens from Mn (99.9% pure) chips and Sn (99.8% pure) foil. All alloy specimens were then polished to a 0.3 μm finish using silicon carbide paper followed by alumina colloidal powder suspension on all sides. Four samples were used for each condition to ensure statistically significant results.

Two sets of four NiMnSn samples were coated with ten bilayers of Poly[Allylamine Hydrochloride] and Poly[Acrylic Acid] ([PAA/PAH]) electrolytic polymer using layer-by-layer assembly via dip coating. One of the sets was left in the uncross-linked stated while the other was heat treated at 200ºC for 2 hours under argon to induce crosslinking of the PAH/PAA coating. To measure coating thickness, P-doped,

single-side polished, <100> oriented silicon wafers from University Wafer were coated in a similar manner and ellipsometry performed to determine the thickness of the crosslinked and uncrosslinked films. Film thicknesses were measured using a Model alpha-SE Ellipsometer from J.A. Woollman Co., Inc with a 632.8 nm laser and a 70º incidence angle. The uncrosslinked coatings measured 38.0 nm thick while the crosslinked coating measured 27.8 nm after heat treatment.

To assess the cytocompatibility of alloy samples, NIH/3T3 mouse fibroblasts, a cell line commonly used in cytotoxicity studies [36-39], were embedded in three-dimensional poly(ethylene glycol) diacrylate (PEGDA) hydrogels to mimic the cellular environment provided by implant-contacting tissues. Figure 5 displays a schematic of the experimental setup for cytotoxicity experimentation. For both coated and uncoated NiMnSn MSMAs, cytotoxicity assessments were correlated with alloy ion release measures to understand the primary source of observed cytotoxicity. To our knowledge, this study presents the first cytotoxicity evaluation of NiMnSn MSMAs with and without a polyelectrolyte passive coating.
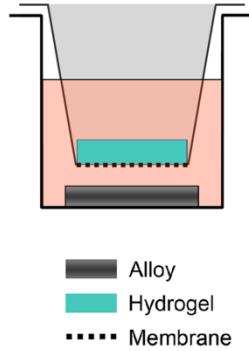
Figure 5. Schematic showing the submerged alloy sample and hydrogel that contains the cells used for study.

2.3 Results and Discussion

2.3.1 Magneto-Thermo Response of Porous NiCoMnSn MMSMAs

These experiments test the coupling between the magnetic and thermal energy domains. Characterizing this response will help determine the effects of processing on the martensitic transformation and ensure that we can obtain magnetic field induced phase transformation (MFIPT) for our target applications. Figure 6 compares the magnetization response as a function of temperature for a homogenized sample (solid red) fabricated by heat treating a sample in a sealed quartz ampule with porous samples created with (green solid) and without (blue dashed) an oxygen getter. Focusing on the 0.05T curves for the homogenized and getter samples, a shift in the magnetization from 35 emu/g to almost 0 emu/g between 320K and 290K during cooling under 0.05 T is observed as the material undergoes a first order phase transformation from partially magnetized ferromagnetic austenite to weakly magnetic self-accommodated martensite. Further cooling to 100K does not produce a significant change in the magnetization of

19

the martensite phase. Upon heating, the magnetization follows the cooling path in reverse until it increases from 0 emu/g to 35 emu/g between 310K and 335K as the transformation from self-accommodated martensite to austenite occurs. Further heating to 375K follows the same magnetization path as the initial cooling curve. The martensite start (M_s), martensite finish (M_f), austenite start (A_s) and austenite finish (A_f) temperatures taken from this curve using the slope intercept method are 315K, 299K, 319K and 333K respectively.
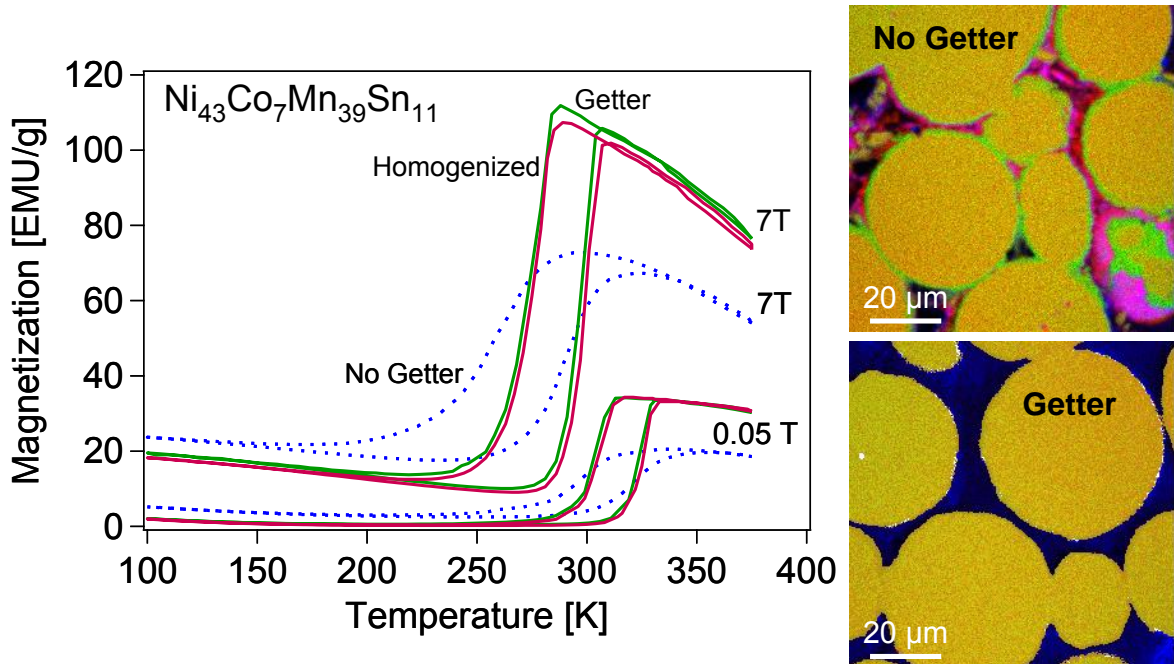
Figure 6. Magnetization as a function of temperature at 0.05T and 7T for the homogenized powder and porous samples fabricated with and without an oxygen getter. X-ray maps of the sample heat treated without, top right, and with, bottom right, an oxygen getter where yellow is the nominal alloy composition, green is a Mn poor phase, purple in Mn oxide and blue is epoxy used to mount the samples.

Figure 7 displays the extracted martensitic transformation temperatures for the homogenized, getter and no getter samples. The martensite start temperatures for all

samples and the martensite finish temperatures for the homogenized and getter samples fall within a 10ºC temperature window for their respective transitions while the no getter sample's martensite finish temperature is almost 50ºC below the others. This shows that both foams begin transforming at the same temperature, but the oxygen contaminated foam requires much more undercooling to finish the transformation. The thermal hysteresis is also larger and the austenite saturation magnetization is much lower for the oxygen contaminated specimen. The x-ray maps on the right of Figure 6 show the strut microstructure of the porous materials after sintering. It is believed that the Mn-oxide and Mn depleted regions surrounding the powder particles do not undergo martensitic transformation and act as a barrier to martensite propagation. This is the cause for the increased hysteresis and significant amount of undercooling required for complete martensitic phase transformation. The response almost identical to the homogenized sample was achieved by sintering with a Ti getter that has a higher oxygen affinity than any of the MMSMA's constituent elements and allowed fabrication of the alloy with no detectable oxygen contamination.
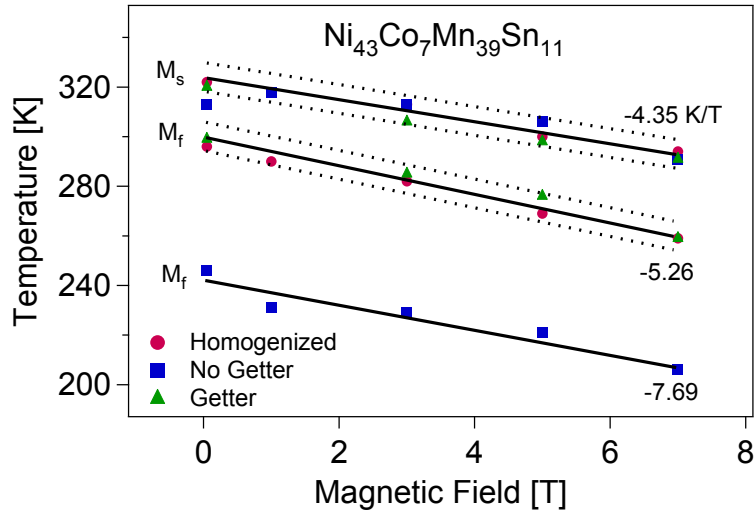
Figure 7. Martensite start (M$_s$) and finish (M$_f$) transformation temperatures for the homogenized, no getter and getter samples.

Figure 8 displays a) the magnetization as a function of applied magnetic field at 280 K, 290 K, 300 K and 310 K and b) the austenite start (A$_s$) relationship between temperature and magnetic field for the porous sample processed with the oxygen getter. These temperatures were selected to be below the material's A$_f$ in order to show magnetic field induced phase transformation (FIPT). The specimens were cooled to 150 K under 0 T before each test to ensure the material was fully martensitic prior to magnetic loading. At 280 K, the constant slope and absence of hysteresis as the magnetic field is increased to then decreased from 7 T indicates that the material remains fully in the paramagnetic/antiferromagnetic martensitic state at this temperature. In comparison, the magnetization for the 310K test deviates from the 280K response below 1 T as austenite is nucleated within the self-accommodated martensite. Increasing the magnetic field above 1 T, the magnetization increases rapidly as the ferromagnetic austenite phase

grows at the expense of the weakly magnetic martensite. The magnetization then saturates at 105 emu/g as the transformation from weakly magnetic martensite to ferromagnetic austenite is completed. This value, shown by the dashed line, is the same as the magnetization at 310 K for the 7 T heating-cooling curve in Figure 6. As the magnetic field is ramped down the material remains mostly austenitic until 2 T as shown by the almost constant saturated value. Just below 2 T, the magnetization begins to drop rapidly as the material begins to transform back to martensite. It is unknown directly if the transformation is fully reversed as the magnetization for both austenite and martensite go to zero as the field is reduced to 0 T. The tests at 290K and 300K show the same MFIPT as the 310K test, but the absence of a magnetic saturation response indicates an incomplete transformation. The A_s temperatures were determined for the 290 K, 300 K and 310 K tests using the slope intercept method as shown in the Figure 8a.
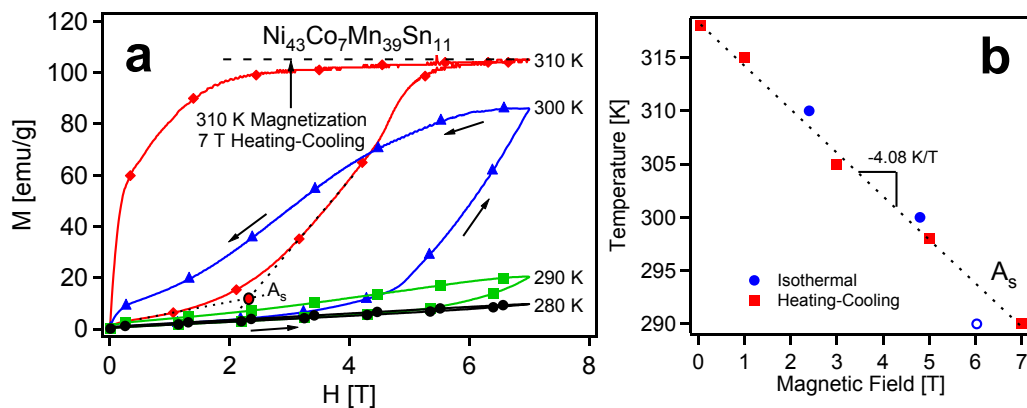
Figure 8. Magnetization as a function of magnetic field, a), and the critical austenite start (As) temperature and magnetic field extracted from Figure 3.

Figure 8b displays the critical A_s values taken from Figure 6. The linear A_s response in Figure 8b shows a constant Clausius Clapeyron relationship with a -4.08 K/T slope:

$$\frac{dT}{dH} = -\frac{\Delta M^{A \rightarrow M}}{\Delta S^{A \rightarrow M}} \qquad (1)$$

Where T is temperature, H is magnetic field, S is entropy and M is magnetization. Using ΔS values of 22.48 J kg^{-1}K^{-1} calculated from differential scanning calorimetry experiments (not shown here), and estimating ΔM to be 100 emu g^{-1} from Figure 6, the predicted CC relationship is $\frac{dT}{dH} = -4.45$ K/T which is comparable to the value experimentally derived from SQUID measurements.

2.3.2 Thermo-Mechanical Response of Porous NiCoMnSn MMSMAs

2.3.2.1 Heating-Cooling

These experiments examine the effects of strut density on the thermo-mechanical coupling of the NiCoMnSn alloy foams. This helps determine the optimal parameters for obtaining a MMSMA foam with high fracture strength and large actuation strains. Figure 9 depicts the thermo-mechanical response for three 50% 300-500 μm porous specimens with a) 17%, b) 13% and c) 5% strut porosity. The increases in strut density shown in the micrographs were achieved by increasing the sintering temperature and cold compact pressure of the green bodies. Looking at the 20 MPa curve in Figure 9b, the material begins in the fully austenitic state at 380 K and undergoes contraction as the temperature is ramped from 380 K to 340 K. As the material is cooled further, a large increase in strain is observed as the sample undergoes an austenite to martensite transformation. The

24

transformation ends around 300 K where subsequent cooling produces a minor

contraction of the materials as the martensite thermally contracts. Upon heating, the

reverse transformation occurs at a slightly higher temperature causing recovery of the

initial transformation strain. The material does not return to its original strain value at

380 K due to damage and possibly residual martensite that has accumulated during the

forward and reverse transformation.
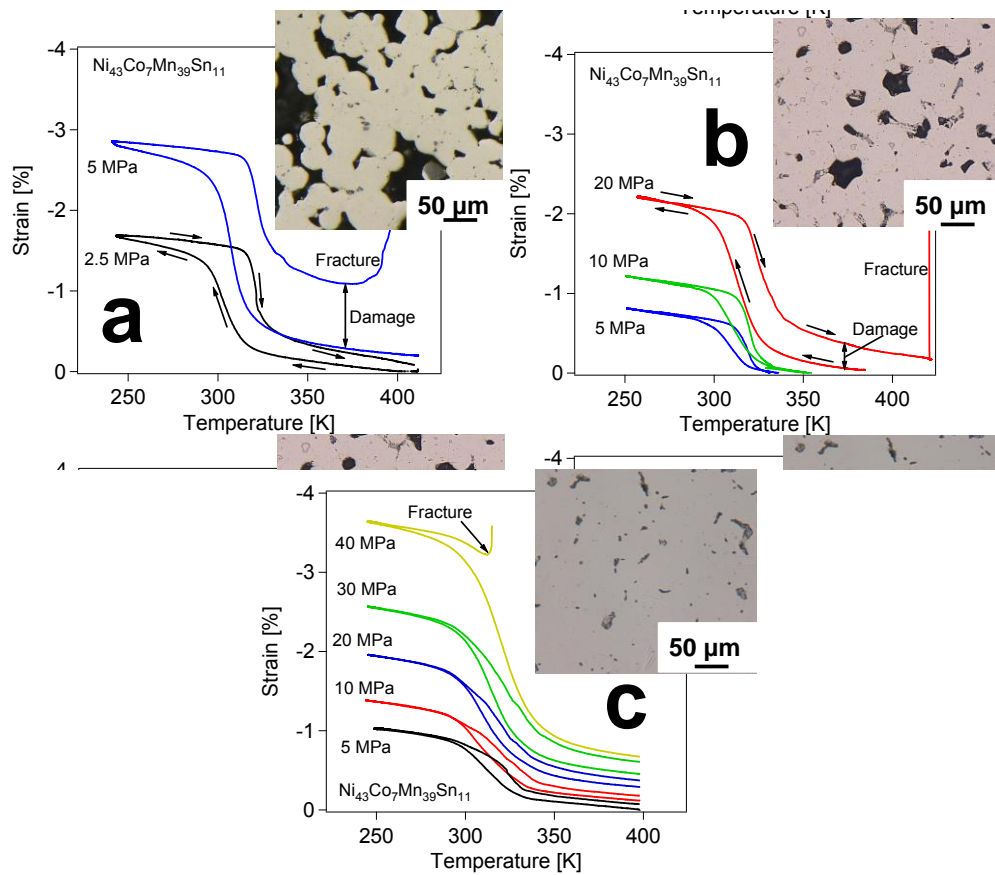
Figure 9. Heating-cooling cycles under constant stress for samples with a) 17%, b) 13% and c) 5% strut porosity.

While full densification could not be achieved, it is easily observed that the increases in strut density decrease the amount of transformation strain and reduce the amount of damage at a given load. The 2% transformation strains observed for each condition prior to failure is comparable to the 3% strains observed in NiCoMnIn single crystal specimens along the [100] direction. This is an encouraging result as it shows that large reversible transformation strains can be achieved in these materials even in polycrystalline form.

2.3.2.2 Superelasticity and Crushing Strength

Figure 10 displays the stress-strain response for a sample with the same strut morphology as shown in Figure 9c. The sample was heated to 65ºC, 10ºC above the A_f temperature, and strained in 0.5% increments up to 2% strain. The material was then heated and a recovery to 0.1% strain was observed. This indicates that a significant portion of the residual strains observed in Figure 9c originate from residual martensite. It is believed that the absence of superelasticity results from residual martensite that is trapped by the grain boundaries in the sample.
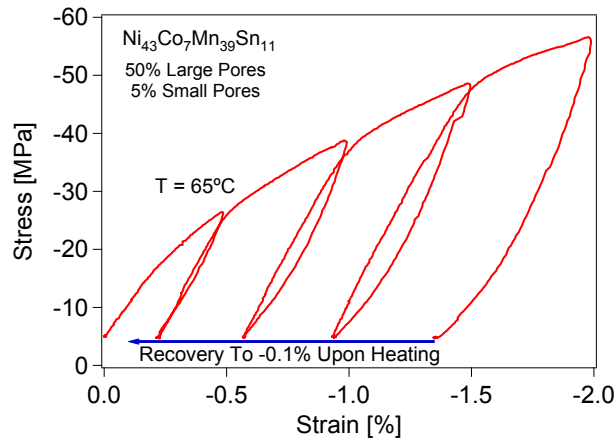
Figure 10. Stress vs. strain showing the shape memory response for a 50% large pore NiCoMnSn with 5% strut porosity as shown in Figure 9c.

2.3.3 Polymer Passivation Layer for Improved Cytocompatibility

2.3.3.1 Cytotoxicity Experiments

Figure 11 displays the cell viability after 7 days of exposure to pure Ni, Mn and Sn and NiMnSn alloy. Viability was significantly lower for cells exposed to NiMnSn relative to cells exposed to Sn (statistical significance level: $p = 0.004$) and relative to media only exposure ($p < 0.001$). The Ni samples were as cytocompatible as the Sn and media-only controls. Cells exposed to pure Mn and NiMnSn alloy samples appear to be of reduced viability relative to media-only controls and are not statistical different from one another. Ion release data (not shown here) indicated that the Ni and Sn controls did not release ions in sufficient quantities to be cytotoxic to the cells used for this study.
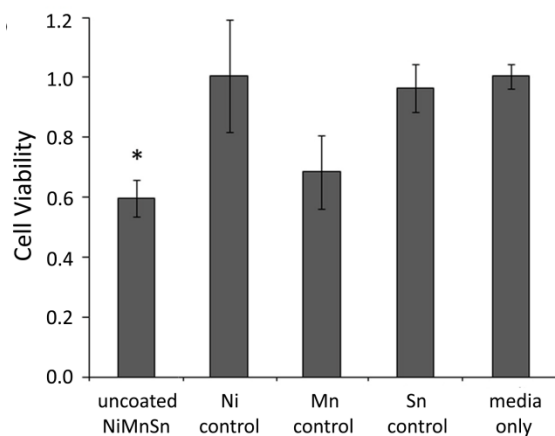
Figure 11. Cell viability for pure Ni, Mn and Sn and uncoated NiMnSn compared to media only.

The cell viability for the coated NiMnSn samples in the crosslinked and uncrosslinked conditions after 14 days are displayed in Figure 12. The uncoated and media only samples are also shown for comparison. The uncrosslinked PAH/PAA coating increased the cytocompatibility of NiMnSn MSMAs by ~36% (p = 0.018). However, thermal crosslinking of the coating degraded the cytocompatibility. The cell viability in the hydrogels exposed to alloys with crosslinked coatings could not be statistically distinguished from that of uncoated NiMnSn samples.
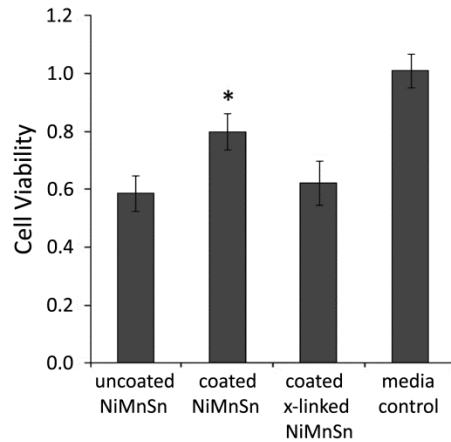
Figure 12. Cell viability for uncoated, coated-uncrosslinked and coated-crosslinked (x-linked) NiMnSn samples.

2.3.3.2 Optical Microscopy

In order to examine the source of this degraded response, optical microscopy, displayed in Figure 13, was performed on the samples before and after the cytotoxicity experiments. One image is shown for day 0 except for the crosslinked-coated group where a defect in the coating is clearly observed in the inset. For the 14 day time point, two images are provided: 1) a defect-free location and 2) a location where corrosion and/or coating degradation was observed. It should be noted that the lamellar structures in the day 14 defect-free image for the crosslinked-coated samples are martensite plates resulting from the elevated temperature processing associated with coating crosslinking and cooling through the martensitic transformation temperature.

The uncoated samples displayed both corrosion-free and oxidized regions after testing. This variability is expected to result from local material inhomogeneity that persisted after the homogenization heat-treatment. On the other hand, defect locations in

the coated NiMnSn samples show surface bubbles indicative of local coating delamination. However, the surface bubbles are inter-connected and there is no underlying surface corrosion.

The defect regions of the crosslinked-coated samples shows delamination, but the bubbles are separate and there is clear oxidation underneath. More importantly, many of the crosslinked-coatings displayed larger corroded regions where the coating was apparently absent. It is believed that these larger defects were caused by coating shrinkage after crosslinking. These results are contrary to the improved barrier response observed for crosslinking these films [40]. It is therefore necessary to examine other crosslinking routes in order to minimize defect formation and ultimately improve cytocompatibility.
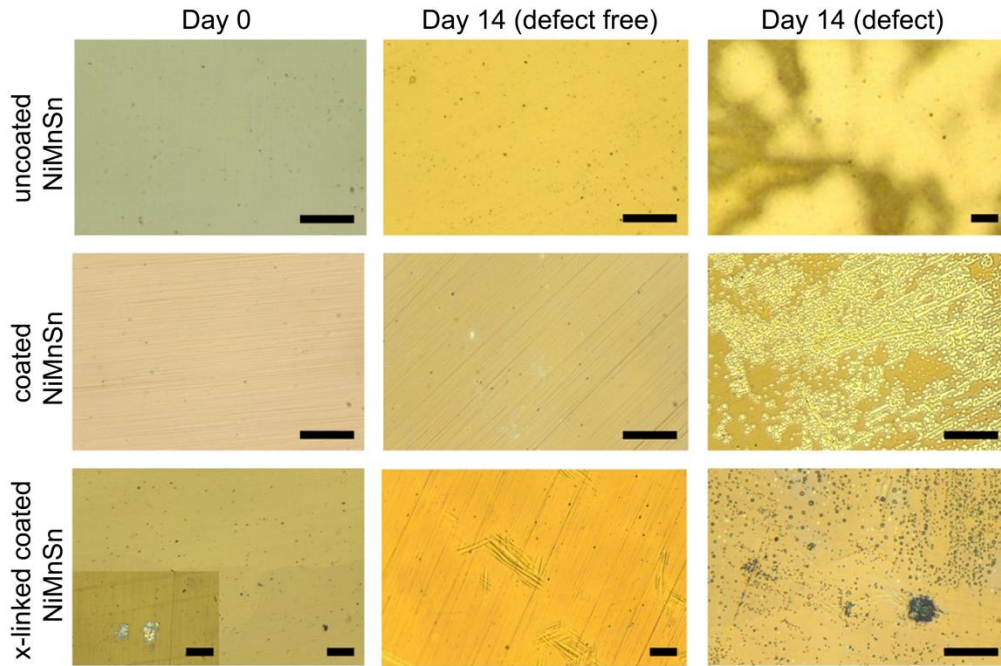
Figure 13. Optical microscopy images of uncoated, coated, and crosslinked-coated NiMnSn samples at day 0 and after 14 days of immersion in cell culture media. Scale bars represent 50 µm.

2.4 Conclusions

In conclusion, the first NiMn based MMSMA foam showing magnetic field induced phase transformation and thermo-elastic martensite was created using solid state replication. The oxygen contamination from processing was successfully prevented and an ideal magneto-thermo response was achieved. Changing the compact pressure and sintering temperature allowed a variety of strut densities to be tested and the first thermo-mechanical experiments on MMSMA foams were conducted. It was found that increasing the strut density increased the stresses that the material could withstand during thermal cycling. Biocompatibility experiments showed that uncoated NiMn based

materials are cytotoxic, but coating them with a passivation layer can successfully reduce cell death by decreasing the amount of corrosion. These findings indicate that these materials can be used in a wider variety of applications by processing them into foams.

CHAPTER III

BRINGING MULTIPLE FERROIC GLASSES INTO FOCUS VIA ORDERING[*]

3.1 Introduction

Glasses are all around us and their properties impact our daily lives. This is reflected in the three material classes (ceramics, polymers and metals) that can form glasses given sufficient quenching rates from a melt. In the last two decades, scientists have discovered magnetic, electric and anisotropic structural (dubbed a strain glass) glasses in a variety of unique materials. Although these systems push our "glassy" preconceptions, the same relaxation dynamics and thermodynamics from general glassy theory can describe their behavior. Studying glass formability in these materials allows new experiments impossible to perform in traditional glasses and can potentially contribute to a more unified glassy theory. Most research on all glasses focuses on enhancing glass formation through compositional changes. Here we explore for the first time how changing atomic configurations with simple heat treatments can stabilize both a strain and a magnetic glass in a single alloy composition.

In order to explain the similarities between traditional, magnetic and strain glasses, it is instructive to first examine glass forming silica [41] as an example. Figure 14a schematically shows that a pure molten silicate undergoes an isothermal phase transformation from an amorphous liquid to a symmetric crystal at the melting point

---

[*] Sections reprinted with permission from Monroe, J. A. *et al.* Direct measurement of large reversible magnetic-field-induced strain in Ni–Co–Mn–In metamagnetic shape memory alloys. *Acta Materialia* **60**, (2012). Copyright (2012) Elsevier.

(Tm). The amorphous structure can be stabilized at slow cooling rates by introducing Na defects that frustrate the crystal's long range translational/rotational symmetry. This allows the liquid's amorphous structure to be super-cooled at T* and frozen below the second order glass transition temperature (T_g). The relaxation dynamics follow a Vogel-Fulcher-Tamman type behavior between T* and T_g and an Arrhenius type behavior below T_g. These critical transitions and the resulting relaxation dynamics associated with them are used to characterize glassy polymers, ceramics and metals, but the implications of these amorphous structures is wider reaching still.
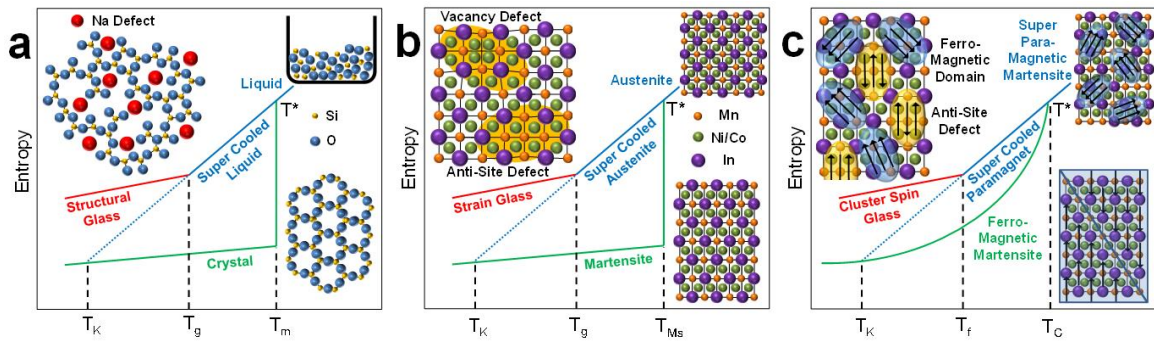
Figure 14. Schematic representations showing similarities between (a) structural glasses, (b) strain glasses and (c) cluster spin glasses. Critical temperatures include melting (T_m); martensite start (T_{Ms}) and Currie (T_C) phase transitions, super cooling (T*), structural and strain glass transitions (Tg), cluster spin glass feezing (T_f) and Kauzmann (T_K).

One can use similar arguments to understand strain glasses even though the transition is between two crystalline solids [6,42-46]. The entropy vs temperature response of a strain glass is shown in Figure 14b. As the austenite phase is cooled, a first order phase transformation to martensite occurs at the martensite start temperature (T_{Ms}). This

34

transformation is characterized by a diffusionless atomic shift from a high temperature crystal phase to a low temperature crystal phase. This is accompanied by local lattice deformation or transformation strains that relate the two phases and produces a deformation that has long range translational/rotational symmetry. If sufficient crystal defects are present, this first order transformation is replaced by a supercooling transition at T* followed by a second order strain glass freezing at T_g. The defects cause local lattice strain along preferred crystallographic directions [47] that produce an anisotropic glassy structure and ultimately frustrate the long range martensitic transformation strain. In other words, the atoms in the anisotropic glass are symmetrically spaced in all directions (like a traditional crystal) except along the austenite to martensite deformation pathway where a non-periodic amorphous structure exists (like a traditional glass). Evidence of anisotropic or strain glasses has been mounting in systems that undergo the martensitic transformation described above. Compositional changes away from stoichiometry impose large defect concentrations in NiTi(Fe, Co, Cr, Mn) [6,44-47], NiCoMnGa [48], and NiCoFeGa [49], NiMnIn(Fe, Cr) [50], CeFe [51], (La, Pr, Ca)MnO3 [51] systems, but the defect identity and the concentrations necessary to stabilize the glassy phase is still unknown.

A similar treatment can be extended to complex magnetic glasses [52] as displayed in Figure 14c. An ordinary ferromagnetic transition in a material with few defects is characterized by magnetic spin alignment along a single direction that creates long range translational/rotational magnetic symmetry. In contrast to the structural systems discussed above, the magnetic symmetry transition is second order and strengthens

during cooling below the Curie temperature (T_c). In a magnetic glass, magnetic defects prevent the local magnetization or spins to form long range translational/rotational symmetry. The asymmetric magnetic structure is supercooled below T* and then freezes below a critical temperature (T_f). These "spin" glasses were first discovered by doping Cu with Mn point defects [53]. In some magnetic glasses, the magnetic point defects form clusters that have local magnetic symmetry but no long range translational/rotational symmetry with each other [8,54]; a structural glass analogy is a semi-crystalline material. Spin and cluster spin glasses have been observed in GdGe [55] and the low temperature martensite phase of CuZnAlMn SMAs [56,57] and NiCoMnSn MMSMAs [8,54].

Although the frustrated microscopic degrees of freedom are wildly different from one another, these glassy systems can be treated in a similar thermodynamic manner at macroscopic scales. One striking similarity is the extrapolated entropy of the high temperature phase intersecting the entropy curve of the low temperature phase in Figure 14a-Figure 14c. At this critical temperature, known as the Kauzmann point (T_K), the high temperature phase's entropy equals the low temperature phase's entropy [58]. This critical point is considered a paradox for structural glasses because it is deemed impossible for a frozen amorphous phase to have lower configurational entropy than a crystalline phase [59]. This is very important for the present discussion as T_K is experimentally determined for our model system.

We show that a Kauzmann point exists in our model alloy system, but here we examine the thermodynamics used to determine T_K. Due to a material's tendency to undergo a glass transition before the Kauzmann point is reached, T_K has only been

directly observed in special cases such as polymer chains with very small breadth-distribution and Helium III and IV [59]. Figure 15 displays a schematic diagram for Helium III or IV adapted from [59] where direct observation of a Kauzmann point occurs in the pressure-temperature phase diagram. The slope of the first order phase transformation line can be used to determine the relative entropy of the two phases by applying the Clausius-Clapeyron relationship $\frac{dP}{dT} = \frac{\Delta S}{\Delta V}$. Firstly, the volume of the liquid phase is assumed to remain greater than the crystalline phase, a reasonable assumption between amorphous and crystalline phases, which makes the ΔV term negative. At high temperatures, the $\frac{dP}{dT}$ slope is positive which indicating that ΔS must be negative and the entropy of the crystalline phase is less than the liquid phase. Similarly, below T_K, $\frac{dP}{dT}$ becomes negative which indicates that ΔS is positive and the liquid phase has lower entropy than the crystalline phase. The point at which the slope changes from positive to negative is defined as T_K and has been calculated to be ~ ½ T_m for many pure metallic elements [58,60]. Another Kauzmann point must exist as the system approaches absolute zero, indicated by the $\frac{dP}{dT}$ slope approaching zero as $T \to 0$, not to violate the third law of thermodynamics [59].

$$\frac{dP}{dT} = \frac{\Delta S^{liq \to crys}}{\Delta V^{liq \to crys}}$$

$S_{crys} > S_{liq}$ | $S_{crys} < S_{liq}$

$\frac{dP}{dT} < 0$

$\frac{dP}{dT} > 0$

T_K

T_K

Crystal

Liquid

$\Delta S^{liq \to crys} = S^{crys} - S^{Liq}$

$V^{crys} < V^{Liq}$

Critical Pressure
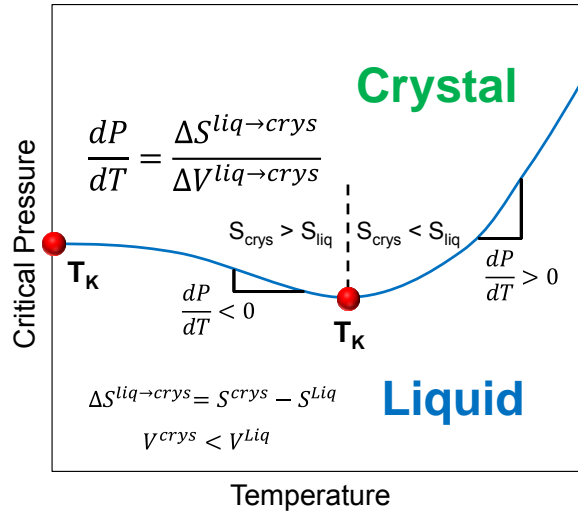
Temperature

Figure 15. A pressure vs temperature schematic for He III or IV displaying the thermodynamic scheme used to determine a Kauzmann point.

NiCoMnIn was selected because it has been studied extensively in the MMSMA literature, can be easily grown into single crystals and is expected to exhibit responses representative of all NiMn based Heusler alloys [7,17,61-67]. Single crystals were used to prevent inter-granular fracture of these brittle alloys and eliminate grain boundary effects on critical transition temperatures. The B2 ordered crystals were subjected to secondary heat treatments between 1073 K and 673 K for three hours to increase the $L2_1$ ordering and defect concentration.

3.2 Experimental Methods

$Ni_{45}Co_5Mn_{36.6}In_{13.4}$ single crystals were grown in a He environment using the Bridgman technique. The crystals were sealed in quartz ampoules and homogenized at 1173 K for 24 hours, then water quenched (WQ). They were then sealed under argon again in quartz ampoules and subjected to secondary heat treatments between 673 K and

1073 K for 3 hours, then WQ. The 673 – 3hr – WQ condition was used for mechanical testing. Single crystal samples were wire electro-discharge machined to 2x2x4 mm3 for uniaxial compression testing and 0.5x2x26 mm3 for dynamic mechanical analysis (DMA) in single cantilever beam mode. The long axes were cut along the [100] crystallographic orientation.

Magnetic properties were measured using a Quantum Design Superconducting Quantum Interference Device – Vibrating Squid Module (SQUID-VSM). All samples were cooled to 5 K under zero magnetic field, a 0.05 T biased field was applied and the sample heated and cooled between 5 K and 400 K. The heating is referred to as the zero field cooling (ZFC) response while the cooling under 0.05 T is referred to as the field cooling (FC) response. Magnetization tests under constant uniaxial compression were conducted using a custom built load cell placed in an extraction type 18 T magnet where magnetization and displacement could be measured simultaneously (see [65] for further details). The sample was loaded to -80 MPa at room temperature, cooled below the martensitic transformation temperature then heated to the desired temperature for magnetization testing. The magnetic field was ramped to and from 18T at 0.3 T per minute. DMA testing was conducted in single cantilever beam mode using a Mettler Toledo TT-DMA. The sample was cooled to 125 K under 0 MPa then heated at 5 K per minute to 400 K while measuring the logarithmically spaced frequency dependent elastic modulus (E') between 0.2 Hz and 25 Hz. The compliance modulus between logarithmically spaced 0.05 Hz and 6.3 Hz was measured at 150 K, 175 K, 200 K and 225 K to determine the characteristic relaxation time (τ_0) at each temperature.

Superelastic compression experiments were conducted on a servo-hydraulic MTS test frame. Cooling was achieved by flowing liquid nitrogen through copper tubes wound around the compression grips while heating was achieved with resistance heating bands wrapped around the copper windings. Displacement was measured by an eddy current sensor that directly measured the gap between the compression grips.

Simultaneous measurements of the magnetization and strain as a function of magnetic field under a constant stress and at different temperatures was achieved with a custom built micro-magneto-thermo-mechanical test frame (micro MTM). The micro MTM's body and inner components are made of precipitation hardened nonmagnetic Cu-Be and can apply compressive stresses on the specimens using 316L stainless steel Belleville springs driven by a screw mechanism. The Belleville springs were specially designed such that the change in applied stress due to thermal expansion during heating/cooling experiments in the temperature range of 300K to 4.2K is not more than ±3 MPa for the given sample dimensions. The level of applied stress remains nearly constant with small variations (±5 MPa) during phase transformation. The device is 10 mm in diameter and 50 mm long which can be used in conventional extraction-type superconducting magnetometers. Displacements during magnetic FIPT with an accuracy of ±0.0001 mm were measured using a miniature capacitive sensor that is capable of measuring the displacement at temperatures as low as 4.2 K and magnetic fields as high as 18 Tesla. The micro MTM was placed in a custom designed extraction type magnetometer with a superconducting magnet to obtain magnetization and MFIS

measurements on the specimens under magnetic fields from 0 to 18 Tesla, test temperatures ranging from 4.2 to 300K and stress levels up to 125 MPa.

Transmission electron microscopy (TEM) samples for dark field imaging were prepared by cutting samples with the [110] zone axis along the beam direction. This was to ensure that the [111] peak that is native to the $L2_1$ structure and systematically absent from the B2 crystal structure. They were then mechanically grinding to 0.1 mm, mounted on Pt TEM holders and electro-polishing.

3.3 Results and Discussion

3.3.1 Ordering Through Secondary Heat Treatments

To date, the strategy to stabilize a strain glass in SMAs has been to add a critical concentration of impurities [45-49]. In this work, we show the same strain glass stabilization can be achieved by manipulating the degree of configurational order in a single alloy composition. Secondary heat treatments on NiMn based MMSMAs between 673 K and 1073 K change the atomic order which in turn changes all the other material transitions. The B2 or CsCl structure displayed in Figure 16a is created when one atom type, Ni and Co in this case, occupy the body centered lattice location and the other lattice sites are another atom type, either Mn or In. This is the ordered structure obtained from quenching the homogenized sample from sufficiently high temperatures. If the sample is held below the B2 to $L2_1$ transition temperature, further ordering to the structure, displayed in Figure 16b, occurs as the Mn and In atoms settle into separate lattice locations.
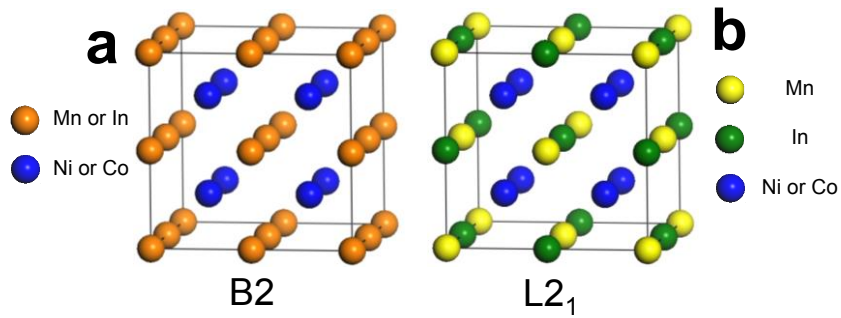
Figure 16. Unit cells for (a) B2 ordering and (b) L2$_1$ ordering observed in NiCoMnIn Heusler alloys.

By holding composition constant, we can examine the strain glass without affecting the alloy's electron-to-atom ratio (e/a ratio) that has a tremendous influence on SMA properties [68]. We also show that configurational order in the same alloy system plays an important role in cluster spin glass stabilization. In order to explore the strain and magnetic glasses in SMAs, we characterized the response of an alloy with Ni$_{45}$Co$_5$Mn$_{36.6}$In$_{13.4}$ atomic percent composition. Different degrees of configurational order, which produce different defect concentrations, were achieved in this off-stoichiometric Heusler alloy through heat treatments between 673 K and 1073 K. These heat treatments affect the material's configurational order and point defect concentration which enhances T$_c$ and T$_f$, suppresses T$_{Ms}$ and ultimately creates a strain glass. T$_K$ is also experimentally determined in a strain glass for the first time.

To obtain a complete L2$_1$ ordered system (Figure 16), a stoichiometric composition of (Ni/Co)$_2$MnIn is required in the NiCoMnIn alloy system. While the selected Ni$_{45}$Co$_5$Mn$_{36.6}$In$_{13.4}$ composition is off this stoichiometry, L2$_1$ ordering still

occurs and can be varied by varying the time and temperature of secondary heat treatments [61]. It should also be noted that the absence of precipitates after secondary heat treatments has been verified through transmission electron microscopy. Constitutional defects such as anti-sites, vacancies and triple defects are expected to increase with greater $L2_1$ ordering due to the off stoichiometric composition. These defects are thought to be the source of the strain and cluster spin glass and can be varied without changing the composition.

3.3.2 Anti-Phase Boundaries

The $L2_1$ ordering has been shown in the literature to occur inhomogeneously in MMSMAs that have the Heusler structure [69]. This creates anti-phase boundaries (APBs) between the $L2_1$ and B2 crystal structures in the material. While the ordering occurs in the parent austenite phase, the daughter martensitic phase inherits the defect structures associated with these APBs. It is believed that the defect structures associated with these APBs and the smaller anti sites lead to the cluster spin and strain glasses observed in these materials. The APB morphology is complex and changes with secondary heat treatment as shown by the dark field images for the 400ºC, 500ºC, 600ºC, 700ºC, 800ºC and 900ºC heat treated samples (Figure 17a – 17f). All the heat treatments a mixture of B2 (dark areas) and $L2_1$ (bright areas) ordering. The 900ºC and 800ºC heat treated samples show $L2_1$ regions that are ~10 nm, but these small regions form larger scale structures shown by Figure 17e and 17f. The 700ºC heat treated sample has a uniform distribution of more refined particles that are ~5 nm and or less. Further decreasing the secondary heat treatment to 600ºC and 500ºC shows coarsening of the $L2_1$ regions to 20-

150 nm and >100 nm, respectively. The 400ºC heat treated sample shows finer regions that are ~20 nm or less. It should be noted that there are no signs of precipitates and the samples contain only B2 and $L2_1$ crystal structures.
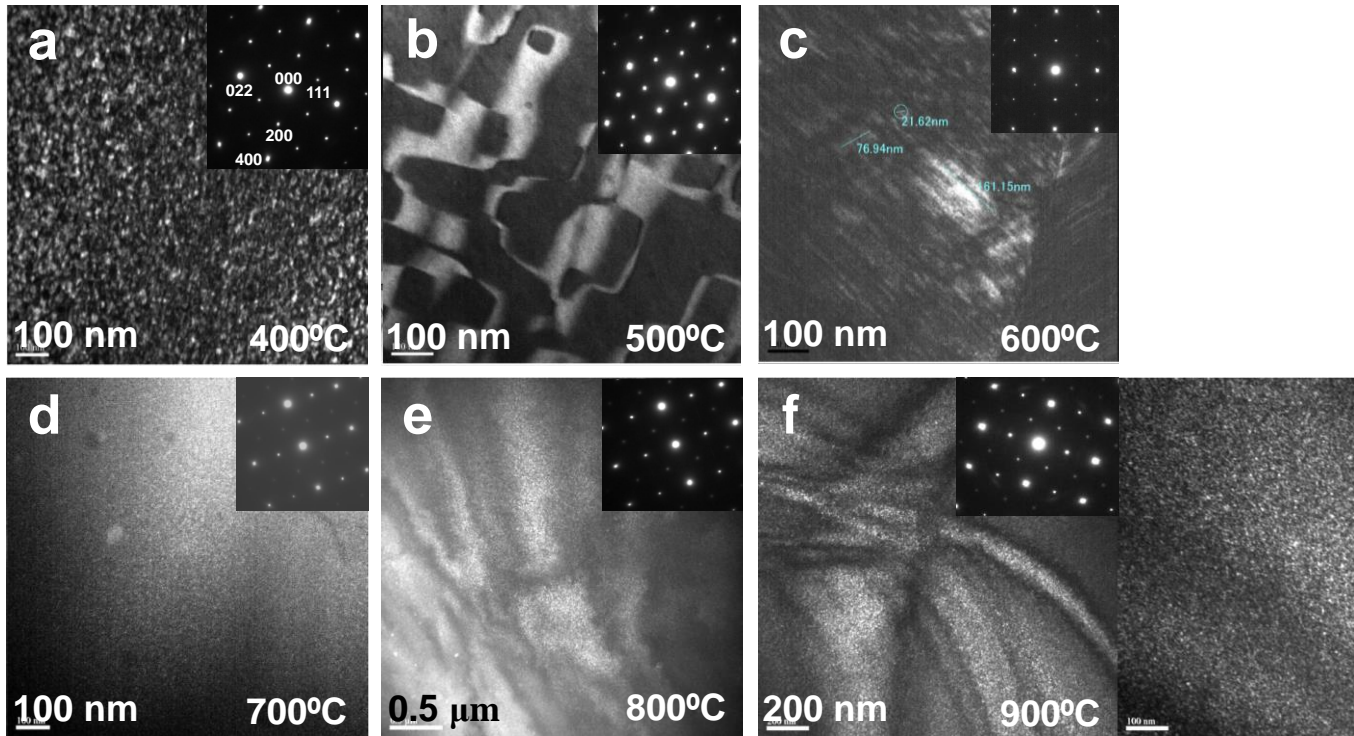
Figure 17. Diffraction patterns and dark field (DF) images of the 111 diffraction peak showing the $L2_1$ morphology (bright regions) for the a) 400ºC, b) 500ºC, c) 600ºC, d) 700ºC, e) 800ºC and f) 900ºC heat treated samples.

3.3.3 Magneto-Thermo Response

3.3.3.1 Zero Field Cooling and Heat Treatment Effects

Magnetization vs temperature plots were used to determine the spin glass freezing (T_f), martensite start (T_{Ms}) and Curie (T_c) temperatures as shown in Figure 18. After zero-field cooling (ZFC), a peak at 33 K is observed in the initial heating response as the 873 K – 3hr – WQ sample undergoes a second order magnetic glass transition at T_f. Further heating causes little change in magnetization until the first order transformation from weakly magnetic martensite to ferromagnetic austenite occurs between the austenite start (T_{As}) and austenite finish (T_{Af}) temperatures. The magnetization then stabilizes until a large transient occurs at austenite's T_c. Upon cooling, the ferromagnetic transition occurs in the austenite with no thermal hysteresis. The austenite to martensite transformation is hysteretic with T_{Ms} and the martensite finish (T_{Mf}) temperature below T_{As} and T_{Af}. The martensite's magnetization is path dependent below T_f. The bifurcation of the magnetization in the ZFC and field cooled (FC) paths is a well-documented phenomenon associated with glassy behavior [52] and results from the spin clusters being frozen in a completely random configuration in the ZFC condition and a biased configuration for the FC condition. A similar response has been observed in the strain response of a strain glass [43] and the electric polarization response of ferroelectric relaxors [70] with the ZFC peak corresponding to glass transition or freezing temperature.
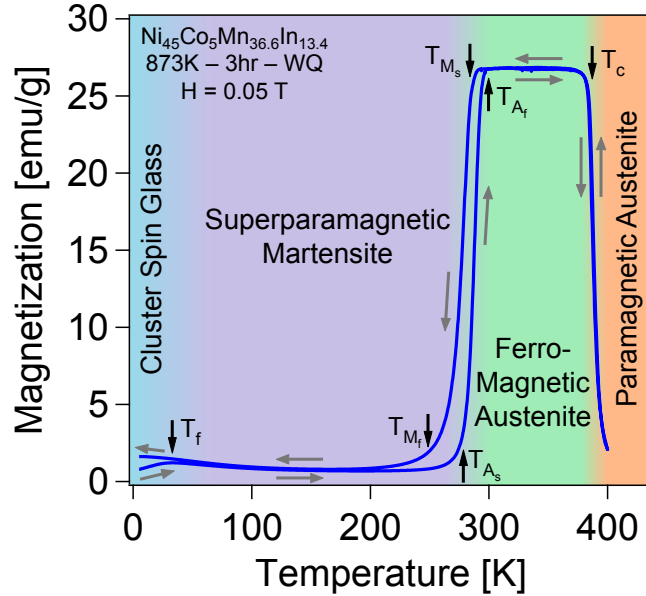
Figure 18. Field heating after zero-field cooling and field cooling magnetization vs. temperature experiments with inflections showing the Currie (T_C), martensitic transformation (T_{M_s}, T_{M_f}, T_{A_s} and T_{A_f}) and path dependent cluster spin glass freezing (T_f) temperatures.
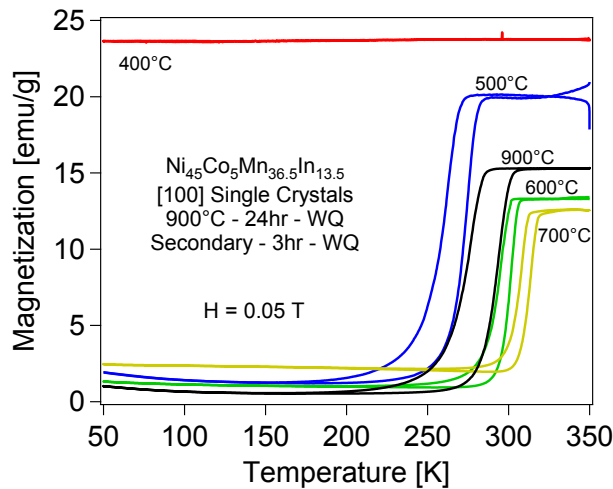
Figure 19. The magnetization as a function of temperature for NiCoMnIn single crystals homogenized at 900C for 24 hours and then subjected to secondary low-temperature heat treatments for 3 hours.

Decreasing secondary heat treatment temperatures increased magnetic transition temperatures, T_c and T_f, and decreased the martensitic transformation temperature, T_{Ms}. Figure 19 displays the magnetization under 0.05 T as a function of temperature for various $Ni_{45}Co_5Mn_{36.5}In_{13.5}$ single crystals homogenized at 900^oC for 24 hours then heat treated at 400^oC, 500^oC, 600^oC or 700^oC for 3 hours. The specimens were heated to 350 K under zero field, the field was ramped to 0.05 T and the specimen was cooled and heated at a rate of 5 K/min. For all samples, except the 400^oC heat treated condition, the magnetization for the austenite remains constant during cooling until a transient due to martensitic transformation is observed. From these experiments, it is evident that the 700^oC secondary heat treatment increases the martensitic transformation temperatures compared to the 900^oC homogenized sample. The transformation temperatures then decrease with decreasing heat treatment temperature while the transformation for the 400^oC heat treated sample does not occur. The change in martensitic transformation temperatures is attributed to an increase in the degree of $L2_1$ ordering in the system [61] while the disappearance of the martensitic transformation is attributed to kinetic arrest [7,71].

3.3.3.1 Isothermal Martensitic Transformations

Figure 20a displays thermal cycles between 300 K and 50 K under 1 T, 3 T, 5 T and 7 T constant magnetic fields for a sample heat treated at 500^oC – 1hr – WQ after homogenization. The transients in magnetization caused by the transformation from magnetically saturated austenite to SAM shift progressively to lower temperatures as the magnetic field is increased to 1 T, 3 T and 5 T. The increasing magnetic field is also

47

accompanied by increases in thermal hysteresis and magnetization values below 100 K. These changes in thermal hysteresis and magnetization are believed to be due to the kinetic arrest of the austenite to martensite phase transformation [7,71,72]. A good example of kinetic arrest and isothermal martensitic transformation is shown when the magnetic field is increased to 7 T in Figure 20b. Like all the previous tests, the material is fully austenitic at 300 K. As the material is cooled under 7T, the material remains austenitic until 170 K where the austenite to SAM transformation begins. As the material is cooled below 170 K, the transformation continues in a step like fashion as martensite variants nucleate and propagate through the specimen in increments. Although the transformation stops at 109 K, shown by the relatively constant magnetization level of 85 emu/g when cooling and heating between 109 K and 50 K, the material is not fully martensitic. In fact, a larger volume fraction of martensite is obtained during further heating as shown by the decrease in the magnetization between 109 K and 130 K. Such austenite to martensite transformation during heating has been referred to as isothermal martensite and in-situ optical microstructural observation has shown that its morphology is much finer than non-isothermal martensite [18,66]. Heating above 130 K produces an increase in magnetization as the martensitic areas of the material transform back to austenite. Although the kinetic arrest is most easily observed in the heating-cooling curve under 7 T, synchrotron diffraction experiments under 3 T and 5 T magnetic fields (not discussed here) have shown the presence of kinetically arrested austenite at low temperatures. This remnant austenite at low temperatures is thought to cause the substantial increase in low temperature magnetization values mentioned previously.

To examine the rate dependent effects and verify that relaxation processes are present in the 7T experiments, Figure 20b shows the magnetization response under 7T for the same sample in Figure 20a, but with various heating-cooling rates. It is evident that the magnetic saturation below 100K increases and the martensite start (M_s) temperatures decrease with increasing thermal cycling rate. This is thought to occur because the faster rate reduces the amount of martensite that can be transformed before the temperature is low enough to arrest the martensitic transformation. The faster rate also causes greater undercooling before the transformation can be observed causing the shift in M_s temperature.
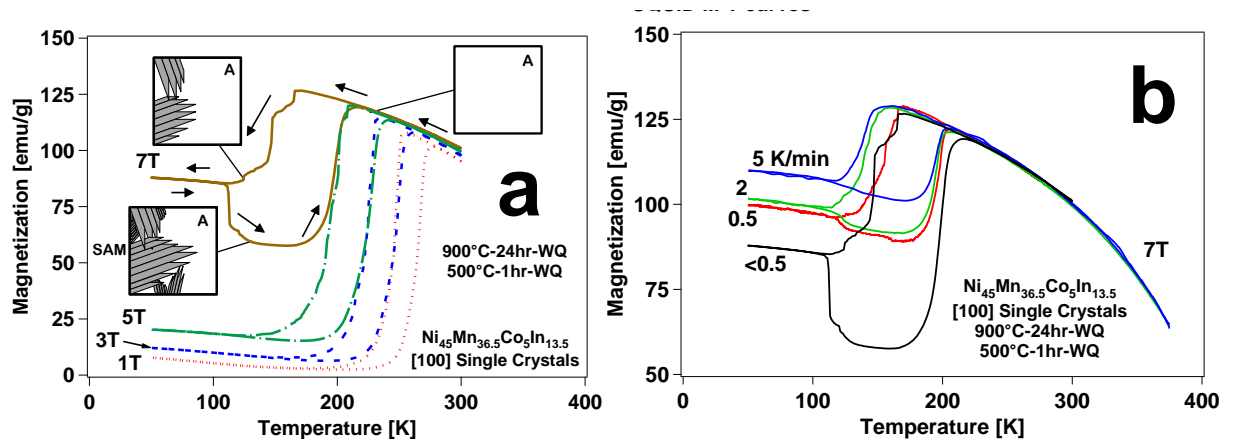
Figure 20. Magnetization as a function of temperature for a NiCoMnIn single crystal stample that shows a) isothermal martensite at 7T and b) the effect of increasing heating-cooling rate on the martensitic transformation.

Lee et al. proposed that the isothermal martensite in NiCoMnIn could be modeled like other isothermal martensitic transitions observed in FeMn steels and constructed a pseudo transformation-temperature-time (TTT) diagram [64]. Interestingly,

similar TTT diagrams can be created for the crystallization of traditional structural glasses. It is thought that the rate dependent experiments, TTT diagram and glass transition are different ways of looking at the same time dependent relaxation problem and the idea of glassiness in MMSMAs and SMAs can be extended to include isothermal martensitic transformations in other material systems. The next section will discuss ways to determine the strain glass freezing point using dynamic mechanical analysis.

3.3.4 Thermo-Mechanical Response

3.3.4.1 Stress-Strain Response of Fully Arrested Condition

Figure 21 displays a) the magnetization vs temperature plot showing of the 400 ºC heat treated sample shown in Figure 19 that shows no transformation up to 7T and b) the same sample showing a non-linear CC relationship with stress induced martensite. This shows that martensitic transformation can be stabilized with stress and that the equilibrium stress has a non-linear relationship temperature. Unfortunately, we are unable to directly observe a Kauzmann point in this response because the stress hysteresis prevents us from determining the equilibrium stress at lower temperatures. It should also be noted that the stress hysteresis that does not allows us to observe the Kauzmann point does not prevent the martensitic transformation as the A_f temperature (T_{Af}) observed during heating after the 133K experiment is well outside the stress hysteresis envelope (σ_{Ms}-σ_{Af}) shown by the 218K experiment.
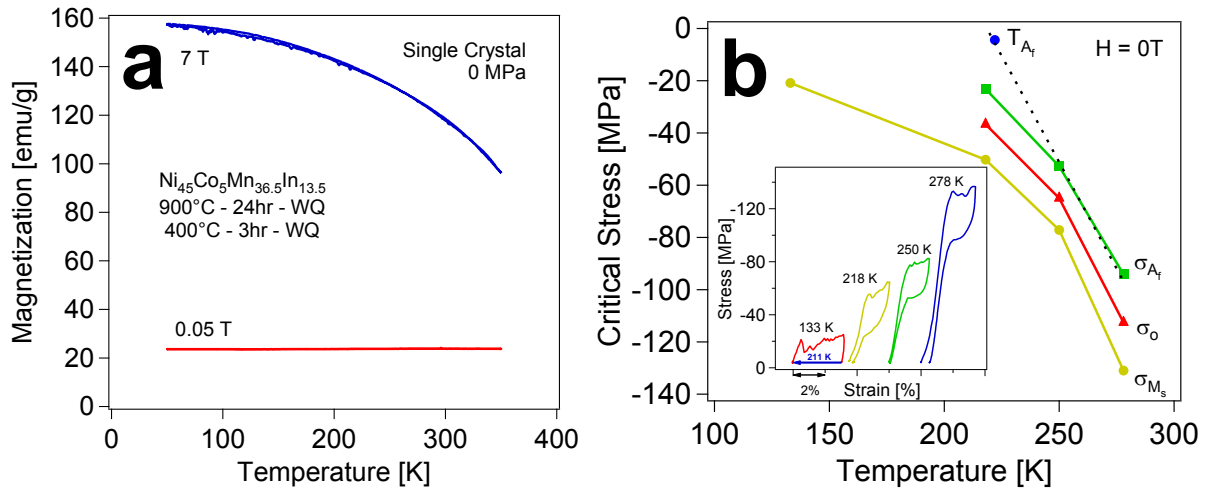
Figure 21. The a) magnetization vs temperature plot showing no transformation for a fully arrested NiCoMnIn sample and b) the same sample showing a non-linear CC relationship with stress induced martensite.

3.3.4.2 Dynamic Mechanical Analysis

T_c could be determined from magnetization tests on the 673 K – 3hr – WQ sample, but T_{Ms} and T_f did not occur when cooling down to 4K because the martensitic transformation was completely suppressed by stabilizing the strain glass phase. This sample condition was subjected to the dynamic mechanical analysis (DMA) displayed in Figure 22 to determine its glassy character. The storage modulus (E') at high temperature is frequency independent and the material stiffens with decreasing temperature. This is expected from a traditional crystalline material. The traditional crystalline response is interrupted by a second order transition (T*) at 261 K followed by decreasing stiffness with decreasing temperature. Clear frequency dependence is also observed during and after the second order transition which indicates a transition from a stable crystal to an

51

unfrozen glass. In contrast, non-glassy SMAs stiffen with decreasing temperature above and below their first order martensitic transformation and any peaks in stiffness occur in the narrow martensitic transformation temperature window [48].
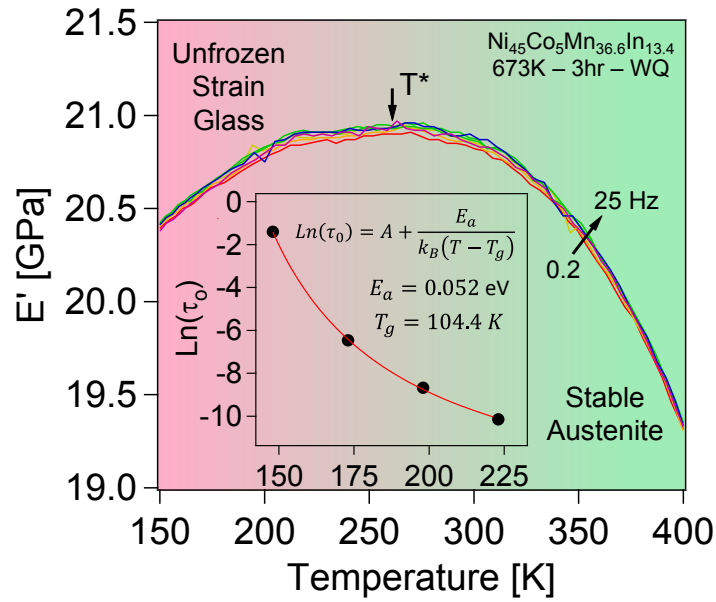
Figure 22. The storage modulus (E') vs temperature showing a frequency dependent second order transition at T* = 261 K. The inset shows a Vogel-Fulcher-Tamman type relationship in the characteristic relaxation time (τ_0) obtained from frequency dependent modulus measurements at four temperatures.

The inset in Figure 22 displays the characteristic relaxation time τ_0 determined using the same frequency dependent compliance scheme introduced in [73]. The relaxation trend has a Vogel-Fulcher-Tamman relationship with temperature; indicative of an unfrozen strain glass with 104.4 K being the ideal glass transition temperature (T_g). This calculation from relaxation experiments coincides with the strain glass transition from direct experiments [73]. The second order transition at T* = 261 K in the main figure is the

52

transition between stable and super-cooled austenite which indicates the 673 K – 3hr – WQ sample is an unfrozen strain glass between T_g and T*.

3.3.5 Experimentally Determined Kauzmann Point

3.3.5.1 Full Magneto-Thermo-Mechanical Testing

To determine the T_K for the 673 K – 3hr – WQ condition and understand its relation to T_g and T*, the martensitic transformation was first stabilized with stress (-80 MPa) and the critical magnetic fields for martensitic transformation were determined at various temperatures. The magnetization (solid) and strain (dashed) vs magnetic field response for the [100] oriented compression sample under -80 MPa is displayed in Figure 23. The -80 MPa load stabilized the martensitic transformation upon cooling in a similar manner to stress induced crystallization in amorphous polymers. Following the 150 K test, the sample begins in the martensitic state at 0 T. The martensite is quickly magnetized to a low saturation point and the strain remains fairly constant as the magnetic field is ramped between 0 T and 3 T. As the magnetic field is increased beyond 3 T the first-order martensitic transformation occurs as evident by the large increase in magnetization and decrease in transformation strain. The transformation is completed around 5 T as shown by the magnetization and strain saturation between 5 T and 10 T. As the magnetic field is removed, the strain and magnetization remain fairly constant and retraces the magnetic loading path until the reverse transformation occurs between 2.5 T and 0.5 T. The critical fields required for martensitic transformation were determined using the slope intercept method shown in the 110K curves. As the testing temperature decreases from 190K to 30K, the critical magnetic field required for the

foreword transformation increases while the critical field for reverse transformation first increases then decreases. These experiments also show that the magnetic saturation of the martensite phase remains lower than the magnetic saturation of the austenite phase down to 30 K.

3.3.5.2 The Kauzmann Point

Figure 24 displays the temperature dependent critical magnetic fields for the martensite start (H_{M_s}) and austenite finish (H_{A_f}) magnetic fields determined from the magnetization and strain measurements given in Figure 23. The equilibrium magnetic field (H_0), defined as the average of the forward and reverse critical fields, is plotted as well. This equilibrium magnetic field is considered to be the equilibrium point in the critical field – temperature phase diagram, Figure 24, because it is rate independent during slowly ramped and rapidly pulsed magnetic field induced phase transformations [66].
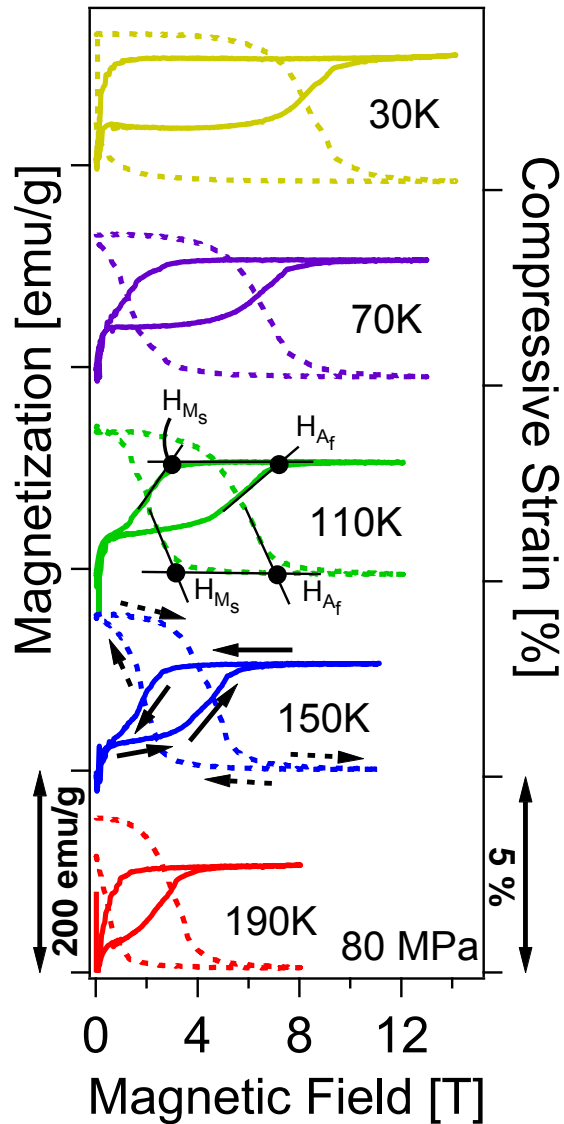
Figure 23. Magnetization (solid) and strain (dashed) measurements vs applied magnetic field for a [100] oriented single crystal in the 673 K – 3hr – WQ condition. Critical transformation austenite finish (H_{A_f}) and martensite start (H_{M_s}) magnetic fields are determined using the slope intercept method.
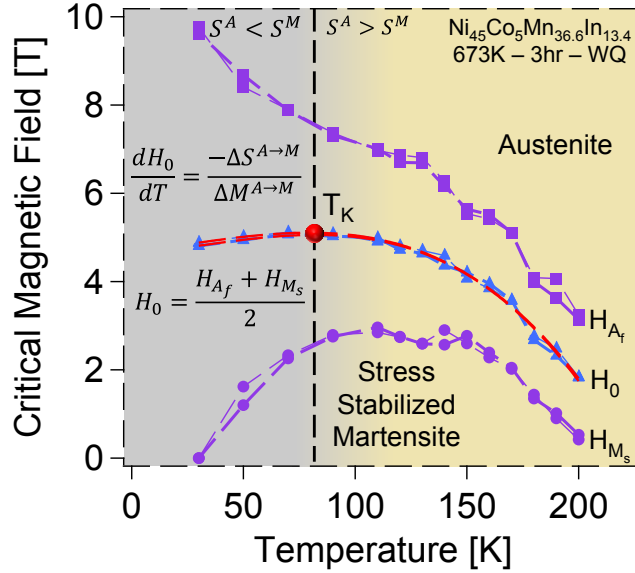
Figure 24. Martensite start (H_{M_s}), austenite finish (H_{A_f}) and equilibrium (H_0) transformation magnetic fields vs. temperature data that show a Kauzmann point at $T_K = 80$ K.

Using the analysis scheme described for Figure 15, a Kauzmann point at 80 K is observed. Here, the temperature dependent slope of the equilibrium magnetic field for phase transformation is used to determine the relative entropy of the two phases by applying the Clausius-Clapeyron relationship $\frac{dH_0}{dT} = \frac{-\Delta S^{A \to M}}{\Delta M^{A \to M}}$; where $\Delta M^{A \to M} = M^M - M^A$ and $\Delta S^{A \to M} = S^M - S^A$ are the difference in magnetization and entropy, respectively, between martensite and austenite. The martenite's magnetization remains lower than autenite's magnetization, evident in the magnetization curves in Figure 23, which makes the $\Delta M^{A \to M}$ term negative throughout the experimental temperature range. Above 80 K, the $\frac{dH_0}{dT}$ slope is negative indicating that the $\Delta S^{A \to M}$ term is negative and thus the autensite phase's entropy is greater than the martesite phase's entropy. As the

temperature decreases, the slope increases until it becomes positive below a critical point at $T_K = 80$ K. This means that under an 80 MPa bias, the austenite phase's entropy is lower than the martensite phase's entropy below 80 K. In other words, the relative thermodynamic stability of the austenite and martensite phases is different above and below 80 K.

3.3.6 Constructed Phase Diagram

The extracted T_c, T_{Ms}, T_f, Tg, T^* and T_K critical transitions for all the samples heat treated between 673 K and 1073 K have been assembled into the phase diagram displayed in Figure 25. To the authors' knowledge, such diversity in material response brought on by simple heat treatments has never been observed in a single alloy composition. The heat treatments between 773 K and 1073 K lead to a transformation sequence similar to the response displayed in Figure 18. In this region of Figure 25, Tc and T_f increase linearly while T_{Ms} decreases linearly with decreasing heat treatment. The samples heat treated between 673 K and 773 K are also similar in response to the sample in Figure 22, but T_f increases exponentially while T_c continues to increase linearly. T_{Ms} first decreases exponentially then rises rapidly indicating unstable supercooling in the gold triangular phase field. The 673 K heat treatment has a very different response that originates from the absence of a martensitic transformation under 0 MPa. Instead of T_{Ms}, a super cooling transition at T^* that falls along the linear extrapolation of T_{Ms}. This gives evidence to T^* originating from a transition between stable austenite and an unfrozen strain glass at the extrapolated T_{Ms} point. The unfrozen strain glass is then expected to freeze below Tg. The T_{Ms} value obtained during cooling under -80 MPa, obtained from

the experiments in Figure 25, displays a continued exponential trend in T_{Ms} allowing completion of the unstable supercooled phase field (gold triangle). While T_K, determined from -80 MPa tests, falls below T_g as expected from the relationship between T_K and T_g in Figure 14.
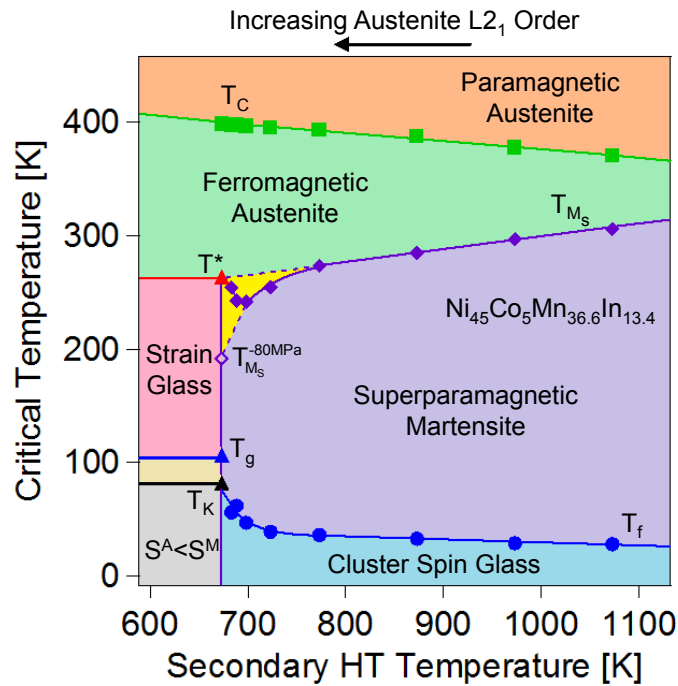
Figure 25. Phase diagram showing the secondary heat treatment influence on the Currie (T_C), martensite start (T_{Ms}), spin glass feezing (T_f), supercooled austenite (T^*), strain glass freezing (T_0) and Kauzmann (T_K) temperatures.

3.3.7 Magnetic Transition Discussion

The degree of $L2_1$ order imparts unique magnetic properties to the Heusler alloys due to the changing Mn atom positions. It is well known from Ruderman-Kittel-Kasuya-Yosida (RKKY) exchange that Mn-Mn atom interactions can be ferromagnetic or anti-

ferromagnetic depending on their distance from one another [74,75]. The average Mn-Mn atom distance in the $L2_1$ structure allows ferromagnetic interaction while the reduced average Mn-Mn distance in the B2 atomic positions couple anti-ferromagnetically [76]. T_C is an indicator of the ferromagnetic coupling strength in a material and thus can be a relative indicator of $L2_1$ ordering. The increases in T_c between the 1073 K and 673 K heat treatments suggests greater $L2_1$ ordering thus confirming the higher ordering shown by diffraction experiments on $Ni_{45}Co_5Mn_{36.7}In_{13.3}$ [61]. While the $L2_1$ ordering occurs in the high temperature austenite phase, the martensite's T_f is still affected because it inherits the austenite's magnetic defect structure. The cluster spin glass in Figure 14c displays a possible ferromagnetic, blue, and atiferromagnetic, yellow, domain structure created by Mn anti-site defects that change the average Mn-Mn distance. While the exact influence of other anti-site, vacancy and other point defects needs to be determined, they would also affect the magnetic domain structure. The higher defect concentration with increasing order stabilizes the cluster spin glass causing the increases in T_f. The exponential increase in cluster spin glass stability between 673 K and 773 K heat treatments indicates the number of defects changes very rapidly within this small heat treatment window. The 673 K heat treated sample does not have a cluster spin glass transition because the strain glass transition stabilizes austenite at low temperatures.

3.3.8 Martensitic and Strain Glass Transition Discussion

Increasing the $L2_1$ ordering stabilizes the austenite phase and pushes T_{Ms} to lower temperatures. The deviation from the linear trend between 773 K and 673 K indicates that the austenite is easily undercooled. This is also evident in the suppressed T_{Ms} for the

673 K sample under -80 MPa. The sudden increase in T_{Ms} for heat treatments very close to 673 K show the complex response of the metastable austenite in the gold colored phase field. The T* transition determined from DMA falls along the linearly extrapolated T_{Ms} curve which strongly indicates that T* is where the austenite becomes supercooled into an unfrozen strain glass. It is proposed that the defects responsible for the anisotropic, or strain, glass are point defects such as the vacancies and anti-site defects shown in Figure 14b. The TEM images showing $L2_1$ morphology within the B2 phase (Figure 17) indicates that a similar defect structures may cause the mirrored exponential decrease and increase in T_{Ms} and T_f, respectively. This is reflected in the anti-site defect illustrations in Figure 14b and Figure 14c.

Studies on the change from an athermal to isothermal martensitic transformation has been studied in the irreversible martensitic transformation of NiMn alloy system by Pati and Cohen [77]. Figure 26 displays the transformation-temperature-time (TTT) showing how decreasing the critical nucleation radius of a matensite nuclei first suppresses the martensitic transformation to lower temperatures and ultimately changes from an anthermal to an isothermal martensitic transformation. It is believed that suppression of the martensitic transformation occurs by a similar mechanism where the element that limits the martensitic transformation is linked to the $L2_1$ morphology. The images shown in Figure 17 indicate that the high temperature heat treatments, 700ºC - 900ºC, result in non-uniform or very fine particles and medium temperature heat treatments show very coarse $L2_1$ particles. The non-uniform areas and very coarse particles allow large martensite plates to form and then propagate very easily through the

single crystals. The 400ºC heat treated sample shows very uniform small of L2$_1$ regions that are thought to decrease the critical martensite nuclei size and result in isothermal martensitic transformations. This is corroborated by TTT diagrams similar to Figure 26 being created for our NiCoMnIn system by Lee et al. [64] and the decreased martensite variant size observed optically in isothermal martensitic transformations by Xu et al. [66]. The transition from athermal (first order) to isothermal (second order) transitions is perfectly described by glassy theory and TTT diagrams are commonly used to describe supercooled and glass forming material systems.
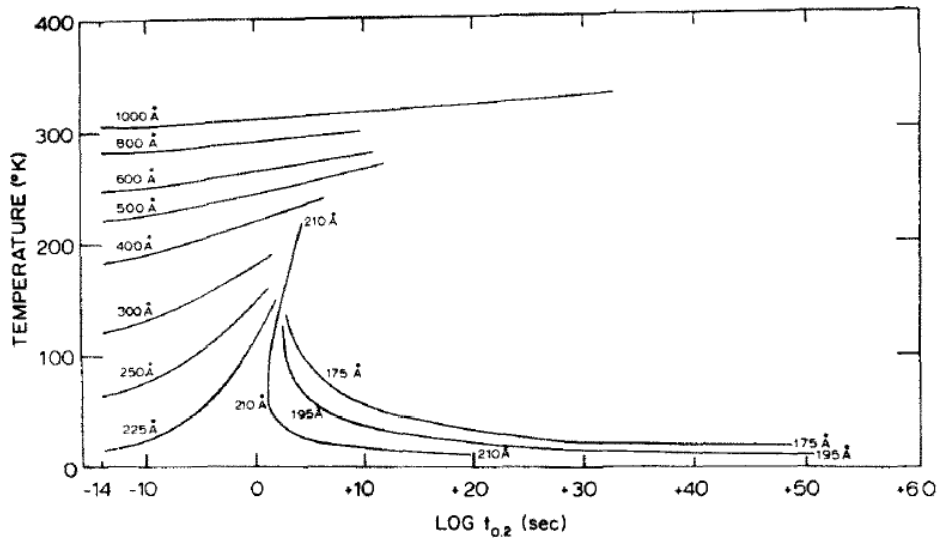
Figure 26. Transformation-Temperature-Time diagram for NiMn based alloy systems developed by Pati and Cohen [77].

Under 0 MPa, the unfrozen glass is expected to freeze below the ideal glass freezing temperature Tg. While Tg above T$_K$ indicates that three external fields (stress,

magnetic field and temperature) to stabilize the phase transformation were required to determine T_K, further testing on T_K's stress dependence must be performed to verify that T_K remains below Tg under 0 MPa. Although they occur close to one another, Tg and T_K may not be co-dependent for these alloys. Indications of T_K have been observed in several MMSMAs that do not undergo a strain glass transition [7,62,67,71]. It has been reasoned that entropy change and resulting thermodynamic arrest in MMSMAs could originate from magnetic contributions [78]. Interestingly, T_K falls along the exponential extrapolation of martensite's T_f from higher heat treatment temperatures, but further investigation of these two phenomena is required to determine if they are linked.

3.4 Conclusions

Glassiness in two functional domains, strain (anisotropic structural) and magnetic, has been observed for the first time in a single alloy composition. The defect structures responsible for the strain and cluster spin glass seem to be similar and are related to crystal structure ordering in the off-stoichiometric Heusler composition. Similar to the progression of traditional glasses, future work should also focus on determining the defect structures responsible for the glassy behavior in these materials in order to allow suppression or enhancement of this glassiness via compositional variations and thermal treatments. A seemingly paradoxical entropy catastrophe known as a Kauzmann point was experimentally observed between two solid alloy phases. These materials provide an excellent model for studying this phenomenon as direct observation of the Kauzmann point is extremely rare in glassy systems. Future work should also focus on mapping the Kauzmann point's dependence on the three intensive

variables; temperature, stress and magnetic field. These endeavors would bring greater insights to the Kauzmann point and general glassy theory.

CHAPTER IV

REVOLUTIONARY TAILORED THERMAL EXPANSION ALLOYS

4.1 Introduction

Materials with negative thermal expansion (NTE) provide interesting technological applications where compensation of positive thermal expansion (PTE) materials is required. Unfortunately, most materials exhibiting NTE have low thermal conductivity and fracture toughness, in the case of ceramics, or the NTE response is only linear over a small temperature range, in the case of invar alloys [79]. Recent research has shown that a large NTE and positive thermal expansion (PTE) response occurs along different crystallographic directions in the martensitic state of NiTi, NiTiPd and NiMnGa SMAs. This has sparked our interest into the unique thermal-mechanical properties of these materials. Manipulating the martenite's texture in these alloys can result in macroscopic NTE materials that are strong, ductile and thermally/electrically conductive. This study aims to create a model for predicting the thermal expansion tensors of these martensitic materials as well as target simple processing routes to allow their use in design and industrial applications.

Thermal expansion anisotropy was observed over a 900 K temperature window in alpha Uranium by Loyd and Barrett [80]. Figure 27 displays the thermal expansion coefficient vs. temperature data they collected. Alpha uranium is orthorhombic and shows positive thermal expansion in the [100] and [001] directions for the entire temperature range shown. The [010] crystallographic direction shows NTE between

975K and 300K and then small positive thermal expansion between 375K and 40K. Interestingly, the thermal expansion anisotropy between 20 K and 40 K changes drastically, as shown by the inset values in Figure 27, where the [100] and [010] directions are both negative and the [001] direction remains positive. It is well known that alpha uranium undergoes a martensitic transformation to a modulated structure at 43 K [81] which indicates that martensitic transformation has a great influence on the material's thermal expansion anisotropy. While these results were collected in 1966, the underlying mechanism for this thermal expansion anisotropy is still not fully understood. More importantly, the use of depleted Uranium is limited in practical applications by its radioactive nature. Understanding the true nature of this thermal expansion anisotropy will allow identification of NTE metals and alloys that are more suited for practical application.
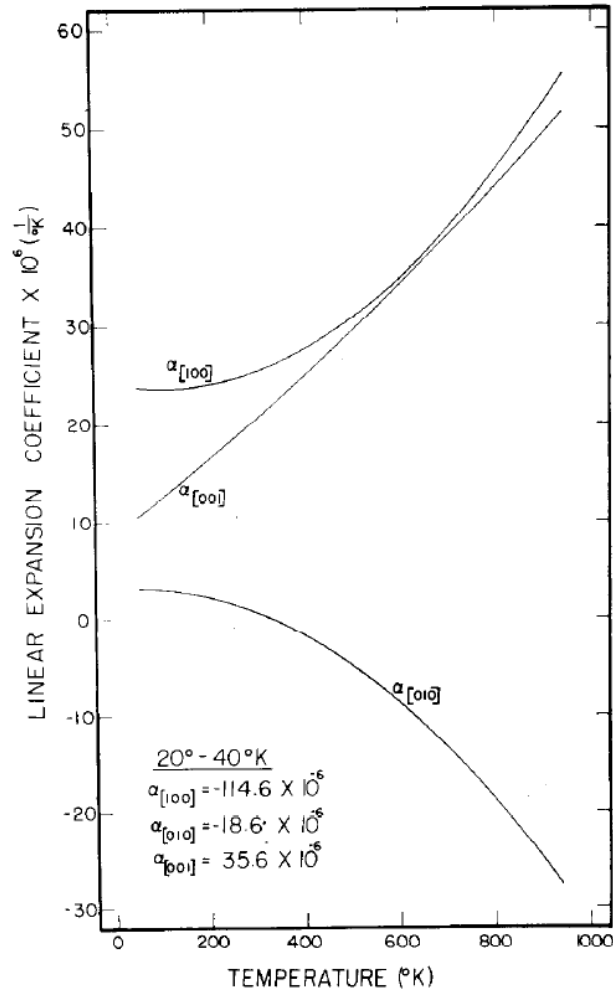
Figure 27. Linear thermal expansion coefficient for alpha Uranium [80].

The traditional SMA NiTi has also shown that the low symmetry monoclinic martensitic phase has a large linear NTE along the a-axis and PTE along the b-axis and c-axis in a 40 K range from neutron diffraction experiments that directly examine the plane spacing of the B19' structure [9]. The heating thermal expansion tensor determined from these experiments is:

$$\epsilon = \begin{bmatrix} \mathbf{-47.2} & 0 & 29 \\ 0 & 43.8 & 0 \\ 29 & 0 & 22.7 \end{bmatrix} \times 10^{-6} \frac{1}{K}$$

This result shows that NTE and PTE anisotropy is not limited to alpha Uranium. It is also important to note the large magnitude of these thermal expansion values. In comparison, mild steel has a thermal expansion coefficient $\sim 12 \times 10^{-6}$ K^{-1} in the same temperature range. Figure 28 gives a graphic representation of the strain directions during heating as they relate to the martensite's monoclinic unit cell as determined by. By taking the Eigen values and vectors of the thermal expansion matrix, we can obtain the principle expansion magnitudes and directions:

$$eig\_value(\epsilon) = \begin{bmatrix} -57.7 & 0 & 0 \\ 0 & 43.8 & 0 \\ 0 & 0 & 33.2 \end{bmatrix} \times 10^{-6} \frac{1}{K}$$

$$eig\_vector(\epsilon) = \begin{bmatrix} -0.94 & 0 & -0.34 \\ 0 & 1 & 0 \\ 0.34 & 0 & -0.94 \end{bmatrix}$$

$\beta \geq 90°$
$\alpha, \gamma = 90°$
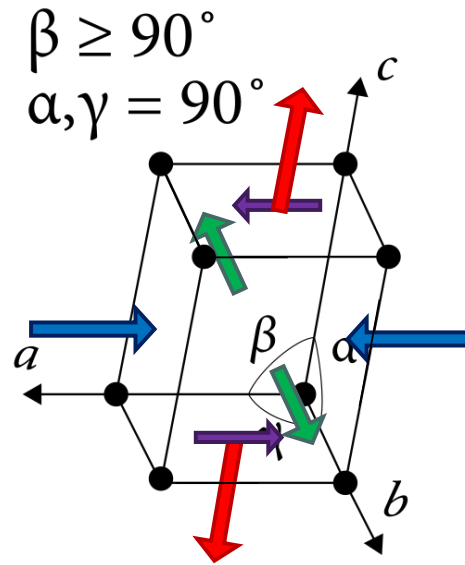
Figure 28. The deformation directions with increasing temperature for the monoclinic martensite of NiTi.

This shows that the maximum linear NTE that can be obtained in martensitic NiTi is $-57.7 \times 10^{-6} \frac{1}{K}$ and the maximum PTE is $43.8 \times 10^{-6} \frac{1}{K}$. By taking the trace of the Eigen thermal expansion tensor we obtain a positive volumetric expansion of $19.3 \times 10^{-6} \frac{1}{K}$ which shows that while we have contraction in one direction, there is an overall volumetric expansion of the martensite with increasing temperature. The Eigen vectors show that only a small counter clockwise rotation about the b axis is required to obtain the principle thermal expansions.

While the thermal expansion anisotropy provides the potential for NTE materials, randomly oriented variants do not provide macroscopic NTE. To observe this behavior, the trace of the principle thermal expansion tensor must be negative; which has not been observed in any of the alloys explored in this work. As a result, processing is necessary

to observe tailored thermal expansion properties at the macroscopic level. Figure 29 displays work by Niinomi et al. [82] where TiNbTaZr biomedical alloys were cold rolled (CR) to between 10% and 90% and the thermal expansion measured. While the authors did not allude to the underlying mechanism for this response, we believe it to be the processing orients martensite variants along martensitic NTE directions.
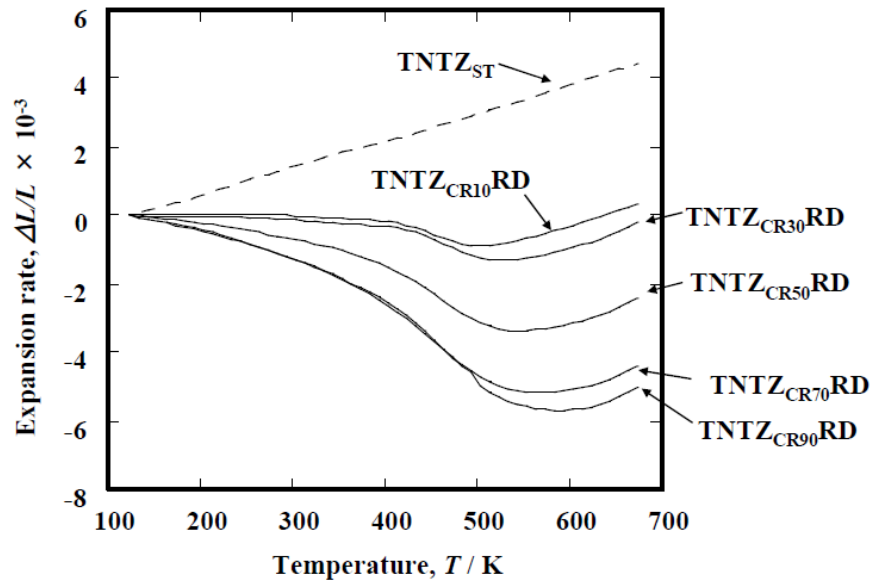
Figure 29. Macroscopic thermal expansion properties of TiNbTaZr shape memory alloys after col rolling from [82].

Clearly, a systematic study of the thermal expansion anisotropy tensors and a model with predictive capabilities is necessary in order to identify various materials with thermal expansion anisotropy. This will then provide materials to explore processing routes that can create alloys with tailored thermal expansion properties. In this work we propose a model to explain the thermal expansion anisotropy, use it to predict the

thermal expansion anisotropy for several alloy systems and use previously published data and advanced diffraction techniques to verify the material response. We then explore processing routes that produce tailored thermal expansion in a NiTiPd model alloy.

4.2 Experimental Methods

$Co_{49}Ni_{21}Ga_{30}$ and $Ni_{45}Co_5Mn_{36.6}In_{13.4}$ single crystal samples were grown for neutron diffraction experiments in a He environment using the Bridgman technique. 4x4x8 mm samples were wire electro-discharge machined (EDM) from the larger single crystals and etched to remove the EMD recast layer. The CoNiGa and NiCoMnIn samples were then homogenized at 1200ºC – 4hr – WQ and 900ºC – 24hr – WQ, respectively, under UHP argon in quartz ampules. For the NiTiPd samples, an ingot of $Ni_{29.5}Ti_{50.5}Pd_{30}$ was vacuum induction melted in a graphite crucible and cast into a copper chill mold. The ingot was homogenized, placed in a mild steel can and hot extruded at 900ºC with an area reduction ratio of 7:1. Specimens for rolling and dogbone tension samples were then wire EDM from the extruded rods.

Lattice parameters were determined using x-ray diffraction (XRD) for NiTiPd and neutron diffraction for the CoNiGa and NiCoMnIn samples. XRD was conducted using Cu K-α radiation on a Bruker AXS X-Ray Diffractometer fitted with a goniometer cradle for texture measurement. Samples were heated in the diffractometer using a hot stage fitted with a platinum resistance heating foil. Figure 30 displays the XRD data taken at 30ºC and 75ºC. The lattice parameters were determined by using a Gaussian fit on the peaks and using Bragg's law to calculate the atomic plane spacing.
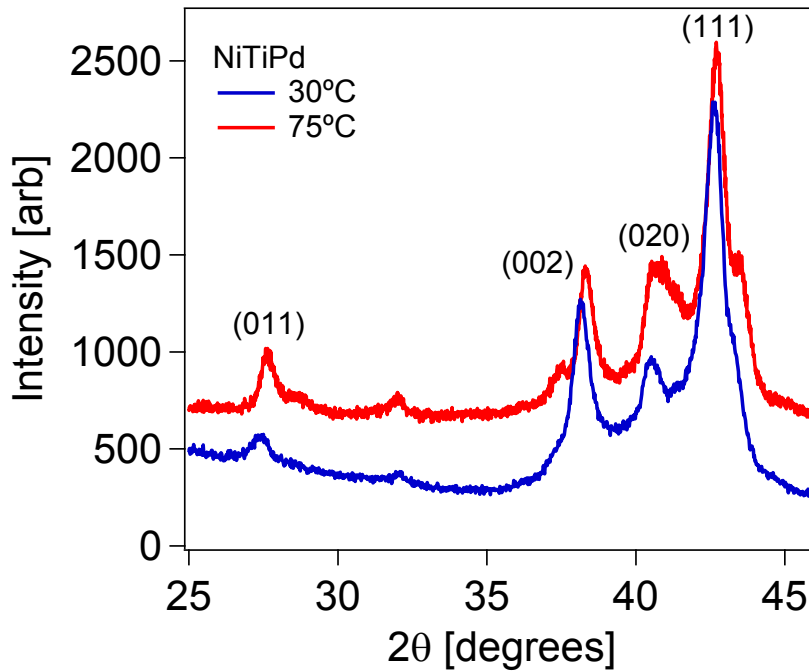
Figure 30. X-Ray diffraction (XRD) of NiTiPd's orthorhombic martensite phase at 30ºC and 75ºC showing the (011), (002), (020) and (111) peaks used to calculate lattice parameters.

Neutron diffraction was conducted at the Spectrometer for Materials Research at Temperature and Stress (SMARTS) facility at the Los Alamos Neutron Science Center (LANSCE). Sample cooling was achieved under vacuum using the low temperature displex hooked up to an intercooler that was capable of reaching temperatures of 50K. Lattice spacing was determined by single peak fits of the time of flight (TOF) data using General Structure Analysis System (GSAS) software. The material's d-spacing at various temperatures was used to calculate the thermal lattice strain and verify the thermal expansion anisotropy. Figure 31 displays examples single peak fit examples in TOF for the martensitic phases of CoNiGa and NiCoMnIn at 50 K.
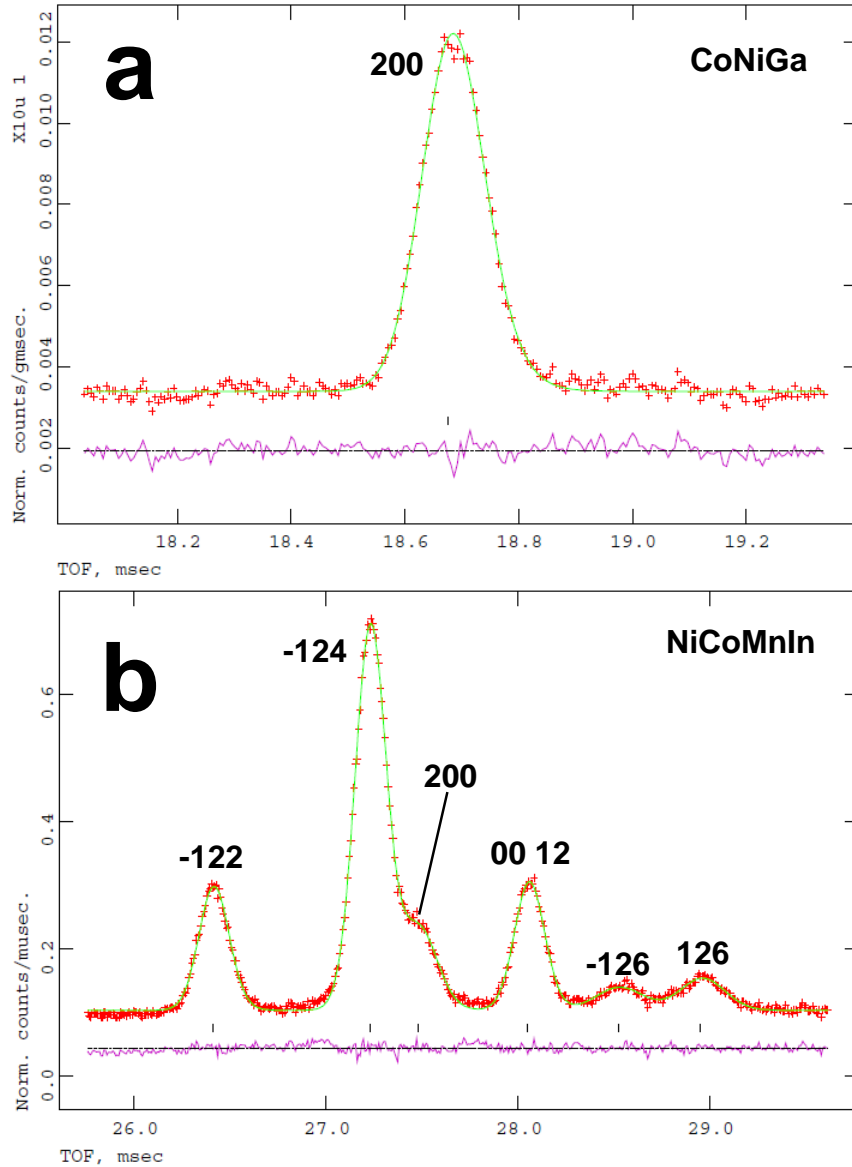
Figure 31. Single peak fits (green) of the neutron diffraction data (red) and the resulting difference curve (pink) for martensitic a) CoNiGa and b) NiCoMnIn at 50 K.

Rolling was conducted at room temperature using a traditional cold rolling system. Percent cold work (CW) was calculated using the change in thickness divided by

the original thickness. Texture analysis was performed before and after CR to observe the change in martensite variant orientation. Samples for thermo-mechanical testing were wire EDMed along the rolling direction (RD) and transverse direction (TD) after CR. The EMD recast layer was mechanically polished and the thermal expansion properties were measured with a TA Instruments Q400 Thermomechanical Analyzer (TMA).

Tensile processing was achieved using a servo-hydraulic MTS test frame. Displacement was measured using an MTS high temperature extensometer fitted with ceramic extension rods in direct contact with the sample. Heating and cooling was achieved by conduction through the grips. Copper coils were wrapped around the grips to flow liquid nitrogen for cooling and band heaters around the coils for heating.

4.3 Results and Discussion

4.3.1 Proposed Mechanism for Anisotropic Thermal Expansion

The proposed mechanism differs from previously proposed mechanisms for NTE in ceramics, metals and polymers. These mechanisms include entropy driven flexible networks, atomic radius contraction and the magnetovolume effect [79]. These are not discussed in great detail here because they differ greatly from the proposed mechanism for NTE in our materials.

It is proposed that while in the low temperature martensite phase, the high temperature austenite phase is constantly sampled by random fluctuations thermal fluctuations. This is similar to the well-established idea that a liquid phase will sample its low temperature crystalline form due to random thermal fluctuations, but this sample

73

is quickly destroyed by other random thermal fluctuations. The sampling rate is dependent upon the free energy difference (ΔG) between the two phases and the temperature at which the sampling is taking place. The free energy difference can be thought of the activation energy for sampling while heat is the energy available for sampling. The sampling will then be a random process that can be described by a probability function:

$$f^A = Be^{\frac{-\Delta G^{M \to A}}{RT}}$$

where f^A is the probability of sampling austenite while in the low temperature martensite state, B is a scaling factor, R is the ideal gas constant, T is temperature and $\Delta G^{M \to A}$ is the temperature dependent difference in free energy between the martensite and austenite phases.

Using the simple rule of mixtures, $f^A + f^M = 1$, and the definition of thermal expansion to be $\epsilon_{ij} = \frac{1}{a_{ij}} \left[\frac{\partial a_{ij}}{\partial T} \right]_{\sigma = Constant}$ the statistical thermodynamic model takes the form proposed by Liu et al.[83]:

$$\epsilon_{ij} a_{ij}(T) = \epsilon_{ij}^M a_{ij}^M(T) + f^A \left(R_{ij}^{A \to M} \left[\epsilon_{ij}^A a_{ij}^A(T) \right] - \epsilon_{ij}^M a_{ij}^M(T) \right)$$

$$+ \frac{\partial f^A}{\partial T} \left(R_{ij}^{A \to M} a_{ij}^A(T) - a_{ij}^M(T) \right)$$

where M designates martensite, A designates austenite, f is the probability function, ϵ_{ij} is the thermal expansion tensor, a_{ij} represents the respective phase's principle d-spacing in Cartesian coordinates and $R_{ij}^{A \to M}$ is a rotation matrix that maps vectors from the austenite to the martensite lattice. This model has been expanded from the previous work

to include anisotropy and collapses to the original equation proposed by Liu et al. [83] if the thermal expansion tensor and d-spacing tensor are assumed to be isotropic (i.e. by replacing the a_{ij} and ϵ_{ij} tensors with V and α scalars, respectively). The rotation matrix is necessary because the crystallographic directions in the austenite and martensite phases are not the same. Figure 32 displays an example for the corresponding lattice coordinates of B2 austenite and L2$_1$ martensite phases. It will be discussed in greater detail in the next section.
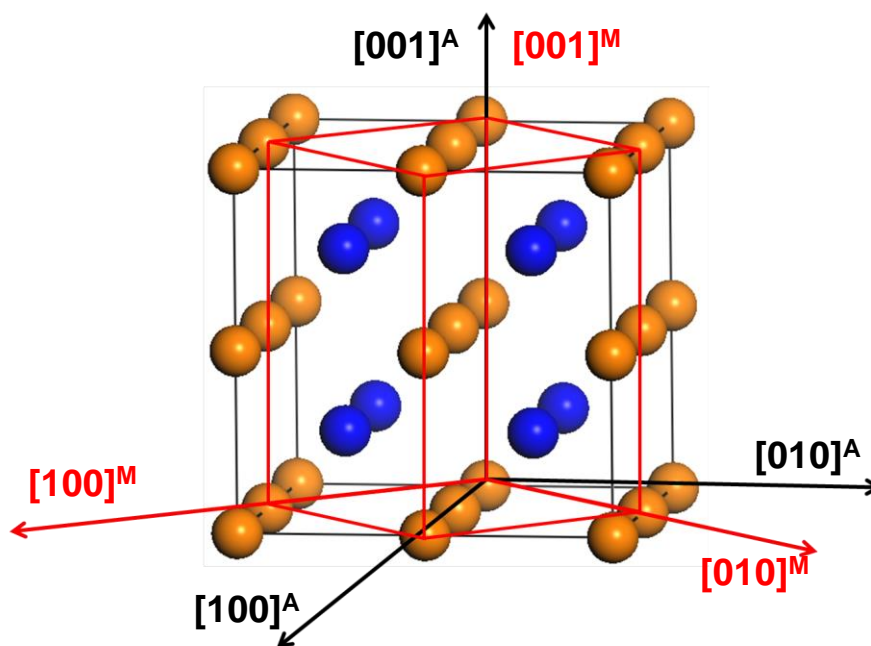
Figure 32. Different matrix coordinates for austenite (black lines) and martensite (red lines).

The first term on the right hand side represents the pure martensite's thermal expansion properties which is expected to be positive in all crystallographic directions. The second term in the right hand side shows the change in thermal expansion properties from replacing the martensite with austenite. Here the austenite thermal expansion properties are also expected to be positive in all directions. The third and final term shows the direct effect of replacing the martensite lattice with the austenite lattice.

In order for negative thermal expansion to be observed, the second term and/or the third term must be negative and sufficiently large to overcome the natural thermal expansion of the pure martensite structure. NTE is obtained along crystallographic directions where the austenite lattice is shorter than the martensite lattice and vice versa. A sufficient criteria for negative thermal expansion along a specific crystallographic direction is of a form also proposed by Liu et al. [83]:

$$f^A\left(1 - \frac{R_{ij}^{A\rightarrow M}\left[a_{ij}^A(T)\epsilon_{ij}^A\right]}{a_{ij}^M(T)\epsilon_{ij}^M}\right) + \frac{\partial f^A}{\partial T}\frac{1}{\epsilon_{ij}^M}\left(1 - \frac{R_{ij}^{A\rightarrow M}a_{ij}^A(T)}{a_{ij}^M(T)}\right) > 1$$

While all parameters for the proposed model have not been obtained, this framework has successfully predicted the thermal expansion anisotropy of six SMAs and alpha Uranium by comparing austenite and martensite lattice parameters.

We will now examine the model in terms of a shape memory alloy system. Taking a closer look at the free energy difference between austenite and martensite, $\Delta G^{M\rightarrow A}$, one can develop a form for the probability function f^A. The free energy difference between austenite and martensite is of the form:

$$\Delta G^{M\rightarrow A} = \Delta S^{M\rightarrow A}dT = \int_{T_0}^{T}\Delta S^{M\rightarrow A}dx$$

where $\Delta S^{M \to A}$ is the difference in entropy between austenite and martensite, T_0 is the equilibrium temperature where the free energy of both phases is equal (i.e. $\Delta G^{M \to A} = 0$) and T is a temperature below T_0. If $\Delta S^{M \to A}$ is assumed to be constant over large temperature ranges (which is reasonable as we examine the constant Clausius Clapeyron slope for most shape memory alloys) the resulting free energy difference is:

$$\Delta G^{M \to A} = \int_{T_0}^{T} \Delta S^{M \to A} dx = \Delta S^{M \to A}(T - T_0)$$

and the resulting probability function is:

$$f^A = B e^{\frac{-\Delta S^{M \to A}(T - T_0)}{RT}}$$

This is important because we can easily observe the effect of constant stress by adding a constant term to $\Delta G^{M \to A}$. This is also important when designing experiments to verify this model because it provides boundary conditions for determining the various constants in the differential equation. It is clear that $f^A \to 0$ as $T \to 0$ or T_0. This means that the two right most terms in the statistical thermodynamic model vanish and the true thermal expansion of the martensitic phase is realized as:

$$\epsilon_{ij} a_{ij}(T) = \epsilon_{ij}^M a_{ij}^M(T)$$

4.3.2 Predicted Thermal Expansion Directions in Various Martensitic Materials

Currently, there is not sufficient data to fit all the parameters in the thermal expansion equation discussed above, but the negative and positive thermal expansion directions can be determined using experimentally determined lattice parameters. Table 3 displays the austenite and martensite lattice parameters for various materials that undergo martensitic transformation. The high temperature austenite phase for all the

materials listed is cubic. These alloys were selected to represent a variety of material

systems (Ni, Co and NiMn based alloys) and marensite crystal symmetry (tetragonal,

orthorhombic, monoclinic and modulated).

Table 3. Lattice parameters in Å for various materials studied. Uranium lattice parameters were obtained from [84].

Phase	Lattice	NiTi	NiTiPd	NiMnGa	Uranium	CoNiGa	NiCoMnIn
Austenite	a^A	3.015	3.091	5.877	3.542	5.743	5.979
Martensite	a^M	4.67	4.697	3.865	2.8535	5.422	4.389
	b^M	4.14	4.450	3.865	5.8648	5.422	5.5784
	c^M	2.91	2.784	6.596	4.9543	6.401	25.932
	β	97.55	-	-	-	-	93.82

The rotation matrix $R_{ij}^{A \to M}$ depends on the transformation path between austenite

and martensite. The corresponding coordinate systems can be related using a simple

rotation around a single axis and can be easily adapted for all martensitic

transformations. Figure 33 shows a typical rotation observed between the austenite and

martensite lattice coordinates. The rotation matrix for this type of transition is given by:

$$R_{ij}^{A \to M} = \begin{bmatrix} \cos\theta & -\sin\theta & 0 \\ \sin\theta & \cos\theta & 0 \\ 0 & 0 & 1 \end{bmatrix}$$

where θ is the angle between the two coordinate systems. As we will see later, different

martensitic transformations will only differ in the stationary axis with direct

correspondence between the coordinate systems. For all the materials studied here, the rotation angle θ is 45º and the rotation matrix is reduced to the form:

$$R_{ij}^{A \to M} = \begin{bmatrix} \dfrac{\sqrt{2}}{2} & -\dfrac{\sqrt{2}}{2} & 0 \\ \dfrac{\sqrt{2}}{2} & \dfrac{\sqrt{2}}{2} & 0 \\ 0 & 0 & 1 \end{bmatrix}$$
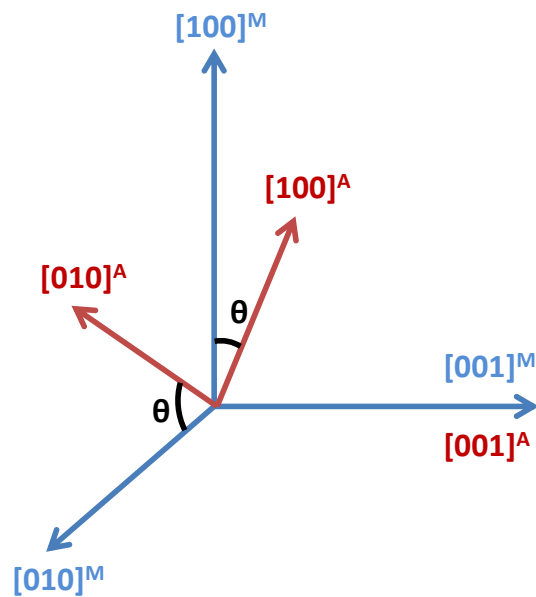
Figure 33. Rotation about the [001] axis (c-axis) from austenite to martensite crystal coordinate systems.

The negative thermal expansion directions can be predicted by applying the rotation matrix to the austenite lattice parameters displayed in Table 3 and observing the crystallographic directions that are smaller than the martensite lattice parameters. Table 2 shows the predicted negative thermal expansion directions, bold and red, based on the

respective expansion matrix and lattice parameters. The crystal structure and lattice

deformation directions expected upon heating are also displayed.

Table 4. Rotation matrix, martensite lattice matrix and thermal expansion tensors for various martensitic materials.

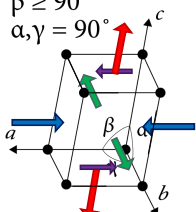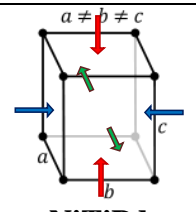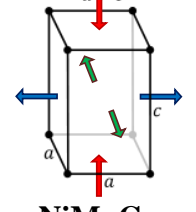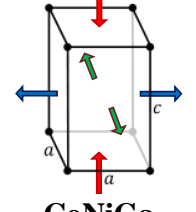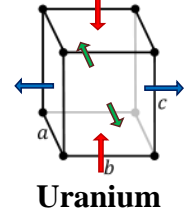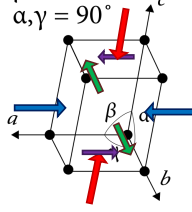| Crystal Structure	Rotation Matrix $R_{ij}^{A\to M}$	Martensite Matrix a_{ij}^M	Thermal Expansion ϵ_{ij}
$\beta \geq 90°$ $\alpha,\gamma = 90°$ **NiTi**	$\begin{bmatrix} \dfrac{\sqrt{2}}{2} & -\dfrac{\sqrt{2}}{2} & 0 \\ \dfrac{\sqrt{2}}{2} & \dfrac{\sqrt{2}}{2} & 0 \\ 0 & 0 & 1 \end{bmatrix}$	$\begin{bmatrix} a^M & 0 & 0 \\ 0 & b^M & 0 \\ 0 & 0 & c^M \sin\beta \end{bmatrix}$	$\begin{bmatrix} \boldsymbol{\epsilon_{11}} & 0 & \epsilon_{13} \\ 0 & \epsilon_{22} & 0 \\ \epsilon_{13} & 0 & \epsilon_{33} \end{bmatrix}$
$a \neq b \neq c$ **NiTiPd**	$\begin{bmatrix} \dfrac{\sqrt{2}}{2} & -\dfrac{\sqrt{2}}{2} & 0 \\ \dfrac{\sqrt{2}}{2} & \dfrac{\sqrt{2}}{2} & 0 \\ 0 & 0 & 1 \end{bmatrix}$	$\begin{bmatrix} a^M & 0 & 0 \\ 0 & b^M & 0 \\ 0 & 0 & c^M \end{bmatrix}$	$\begin{bmatrix} \epsilon_{11} & 0 & 0 \\ 0 & \boldsymbol{\epsilon_{22}} & 0 \\ 0 & 0 & \boldsymbol{\epsilon_{33}} \end{bmatrix}$
$a \neq c$ **NiMnGa**	$\begin{bmatrix} \dfrac{\sqrt{2}}{2} & -\dfrac{\sqrt{2}}{2} & 0 \\ \dfrac{\sqrt{2}}{2} & \dfrac{\sqrt{2}}{2} & 0 \\ 0 & 0 & 1 \end{bmatrix}$	$\begin{bmatrix} a^M & 0 & 0 \\ 0 & b^M & 0 \\ 0 & 0 & c^M \end{bmatrix}$	$\begin{bmatrix} \epsilon_{11} & 0 & 0 \\ 0 & \epsilon_{22} & 0 \\ 0 & 0 & \boldsymbol{\epsilon_{33}} \end{bmatrix}$
$a \neq c$ **CoNiGa**	$\begin{bmatrix} \dfrac{\sqrt{2}}{2} & -\dfrac{\sqrt{2}}{2} & 0 \\ \dfrac{\sqrt{2}}{2} & \dfrac{\sqrt{2}}{2} & 0 \\ 0 & 0 & 1 \end{bmatrix}$	$\begin{bmatrix} a^M & 0 & 0 \\ 0 & b^M & 0 \\ 0 & 0 & c^M \end{bmatrix}$	$\begin{bmatrix} \epsilon_{11} & 0 & 0 \\ 0 & \epsilon_{22} & 0 \\ 0 & 0 & \boldsymbol{\epsilon_{33}} \end{bmatrix}$
$a \neq b \neq c$ **Uranium**	$\begin{bmatrix} 1 & 0 & 0 \\ 0 & \dfrac{\sqrt{2}}{2} & -\dfrac{\sqrt{2}}{2} \\ 0 & \dfrac{\sqrt{2}}{2} & \dfrac{\sqrt{2}}{2} \end{bmatrix}$	$\begin{bmatrix} a^M & 0 & 0 \\ 0 & b^M & 0 \\ 0 & 0 & c^M \end{bmatrix}$	$\begin{bmatrix} \epsilon_{11} & 0 & 0 \\ 0 & \boldsymbol{\epsilon_{22}} & 0 \\ 0 & 0 & \epsilon_{33} \end{bmatrix}$

Table 4. Continued

$\beta \geq 90°$
$\alpha, \gamma = 90°$

NiCoMnIn

$$\begin{bmatrix} \dfrac{\sqrt{2}}{2} & 0 & \dfrac{\sqrt{2}}{2} \\ 0 & 1 & 0 \\ -\dfrac{\sqrt{2}}{2} & 0 & \dfrac{\sqrt{2}}{2} \end{bmatrix} \begin{bmatrix} a^M & 0 & 0 \\ 0 & b^M & 0 \\ 0 & 0 & c^M \sin\beta \end{bmatrix} \begin{bmatrix} \epsilon_{11} & 0 & \epsilon_{13} \\ 0 & \epsilon_{22} & 0 \\ \epsilon_{13} & 0 & \epsilon_{33} \end{bmatrix}$$

The two metallic material systems, discussed in section 4.1, that have shown thermal expansion anisotropy are NiTi and alpha Uranium. Experimentally determined data from neutron diffraction show that NiTi and Uranium have NTE along the [100] and [010] crystallographic directions, respectively, of the low temperature martensitic phase. It is easily seen that the predicted NTE directions using the model's framework can predict the negative thermal expansion directions for two extensively studied materials.

4.3.3 Experimentally Determined Thermal Expansion Tensors

The thermal expansion tensors for CoNiGa, NiCoMnIn and NiTiPd were determined using X-Ray and neutron diffraction to further prove the predictive capabilities of this model. We will see that the predicted NTE directions are realized in each of these material systems even though they each have different crystal structures. It should be noted that experimentally measured terms are $a_{ij}(T)$ which are used to calculate ϵ_{ij}. This is because the diffraction experiments are statistical in nature and only capture the composite response.

4.3.3.1 CoNiGa

Figure 34 displays all the diffraction data collected on CoNiGa between 50K and 290K. The diffraction patterns taken at 5K intervals between 290K and 275K show both austenite (B2) and martensite (tetragonal) peaks. As the temperature decreases, the martensite peaks increase in intensity compared to the austenite peaks showing the volume fraction of martensite is increasing in this temperature range. Austenite peaks are absent from the diffraction patterns between 225K and 50K and there are no significant changes in relative peak intensity. The lattice parameters for the martensitic phase in each of these patterns were used to calculate the thermally induced lattice strain.

Figure 35a shows the first lattice thermal expansion data collected on martensitic CoNiGa and the 250 K temperature window shows previously undiscovered features in the anisotropic thermal expansion response of martensitic alloys. Firstly, the lattice strain is quadratic between 50 K and 260 K. This results in the thermal expansion tensor having a linear temperature dependence as shown in Figure 35b. The thermal expansion tensor between 50K and 225K is:

$$\left(\epsilon_{ij}\right)_{CoNiGa} = \begin{bmatrix} 17.61 + 0.159T & 0 & 0 \\ 0 & 17.61 + 0.159T & 0 \\ 0 & 0 & \textcolor{red}{\mathbf{-20.08 - 0.019T}} \end{bmatrix} \times 10^{-6} \frac{1}{K}$$

which follows the predicted thermal expansion directions from the tensor shown in Table 4. Interestingly, the lattice strain's slope changes sign between 260 K and 300 K. The magnetization vs. temperature curve as well as the diffraction patterns in Figure 34 shows this temperature range contains a mixture of austenite and martensite. While this is not fully understood, it may result from the free energies of the austenite and

82

martensite phases becoming equal as $T \rightarrow T_0$; the temperature where the free energy of

the two phases is equal.
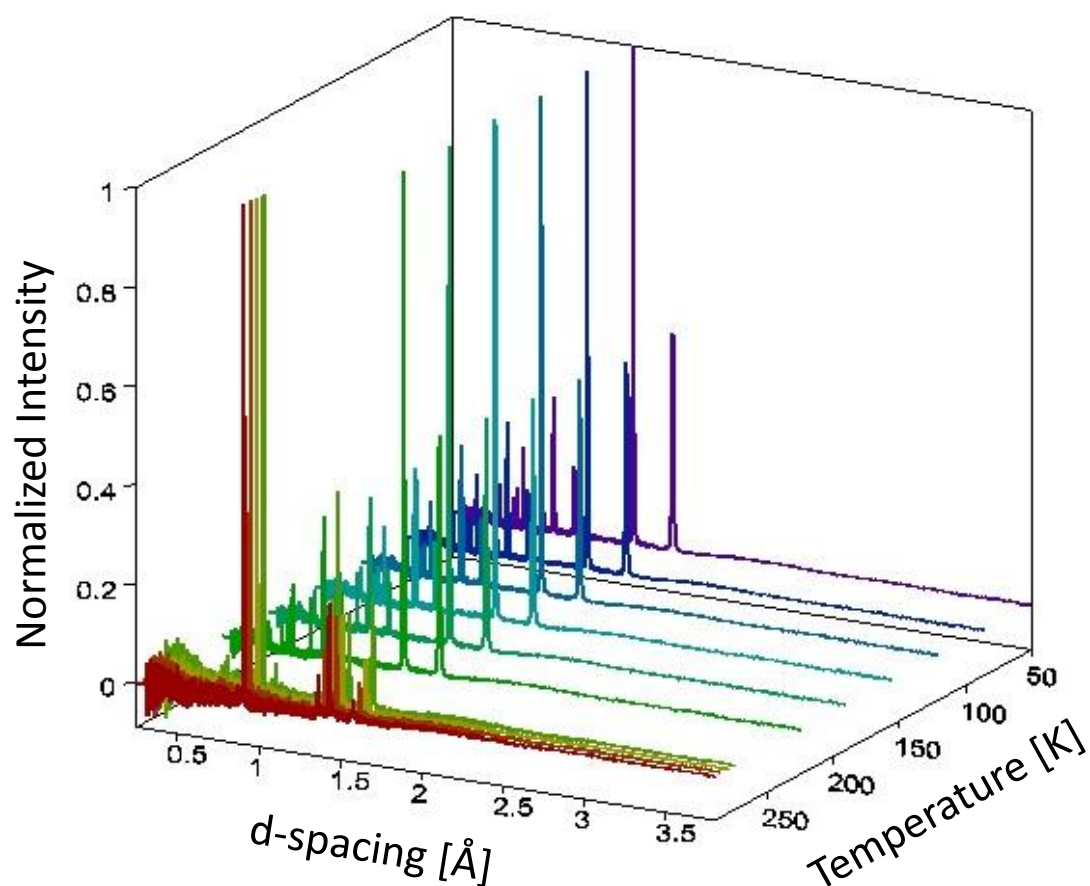
Figure 34. Background subtracted and normalized neutron diffraction data collected between 290K and 50K showing a mixture of austenite and martensite peaks between 290K and 275K and martensite peaks between 225K and 50K.
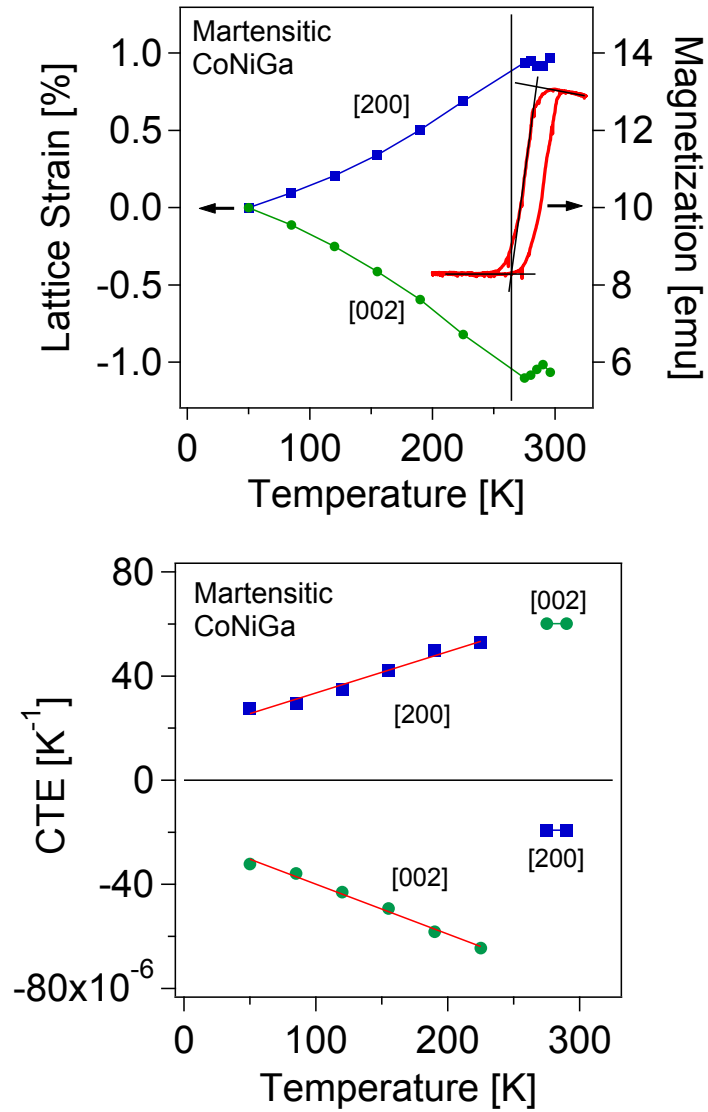
Figure 35. Lattice strain along the [100] and [001] crystallographic directions vs. temperature during heating from 50 K to 300 K. Magnetization measurements showing the location of the martensitic transformation is also shown. Note: [100] and [010] crystallographic directions are equivalent in the tetragonal system.

4.3.3.2 NiTiPd

Figure 36 displays the lattice strain vs. temperature obtained from XRD data for the NiTiPd high temperature shape memory alloy. The resulting thermal expansion tensor for this material between 25ºC and 110ºC is:

$$\left(\epsilon_{ij}\right)_{NiTiPd} = \begin{bmatrix} \epsilon_{11} & 0 & 0 \\ 0 & \epsilon_{22} & 0 \\ 0 & 0 & \epsilon_{33} \end{bmatrix} = \begin{bmatrix} 115.8 & 0 & 0 \\ 0 & -37.34 & 0 \\ 0 & 0 & -41.58 \end{bmatrix} \times 10^{-6}\frac{1}{K}$$

The negative thermal expansion directions match those predicted using the statistical thermodynamic model. The CTE values vs. temperature are not plotted because they are constant for the shown temperature range. More experimentation below room temperature is required to determine if the thermal expansion tensor is linear with temperature as was shown with CoNiGa.
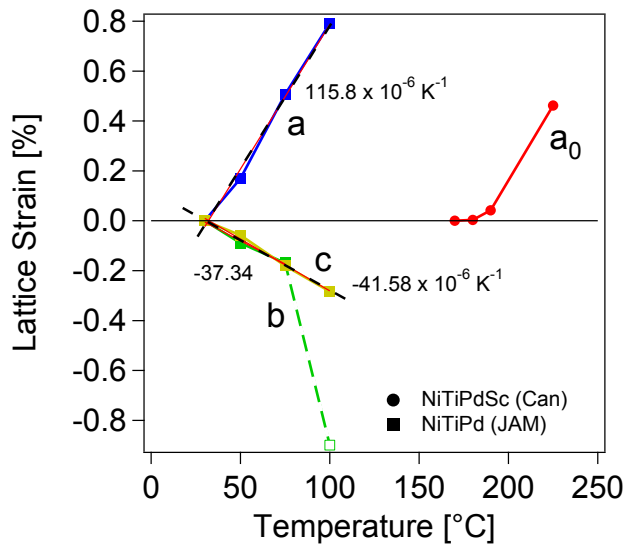
Figure 36. Lattice strain vs. temperature for NiTiPd high temperature shape memory alloy.

4.3.3.3 NiCoMnIn

Figure 37 displays all the diffraction patterns collected on the NiCoMnIn between 50K and 300K. The between 300K and 280K are fundamental peaks from the cubic austenite phase while the large number of peaks between 225K and 50K belong to modulated martensite. Unfortunately, the diffractometer was not able to collect enough peaks from the single crystalline samples to allow Rietveld refinement of lattice parameters. Therefore, the lattice spacing was calculated by averaging the single peak fit d-spacing for low and higher order reflections as well as the two detector banks.

Figure 38 displays the lattice strain along the [200], [00 12] and [126] crystallographic directions for this material. Using the lattice parameters in Table 3, the normal vector in the martensite's coordinate system for the [126] plane is $n_i = (0.47,\ 0.74,\ 0.48)$. From the equation $\epsilon_n = n_i \epsilon_{ij}$ we can derive the equation for the thermal expansion component along the [010] axis to be $\epsilon_{22} = \frac{1}{n_2}(\epsilon_n - n_1\epsilon_{11} - n_3\epsilon_{33})$. Using this equation and the thermal expansion calculated for the [200] and [00 12] planes, the thermal expansion tensor between 50 K and 225 K is:

$$\epsilon_{ij} = \begin{bmatrix} 1.67 & 0 & \epsilon_{13} \\ 0 & -1.99 + 0.062T & 0 \\ \epsilon_{13} & 0 & 2.10 + 0.002T \end{bmatrix} \times 10^{-6}\frac{1}{K}$$
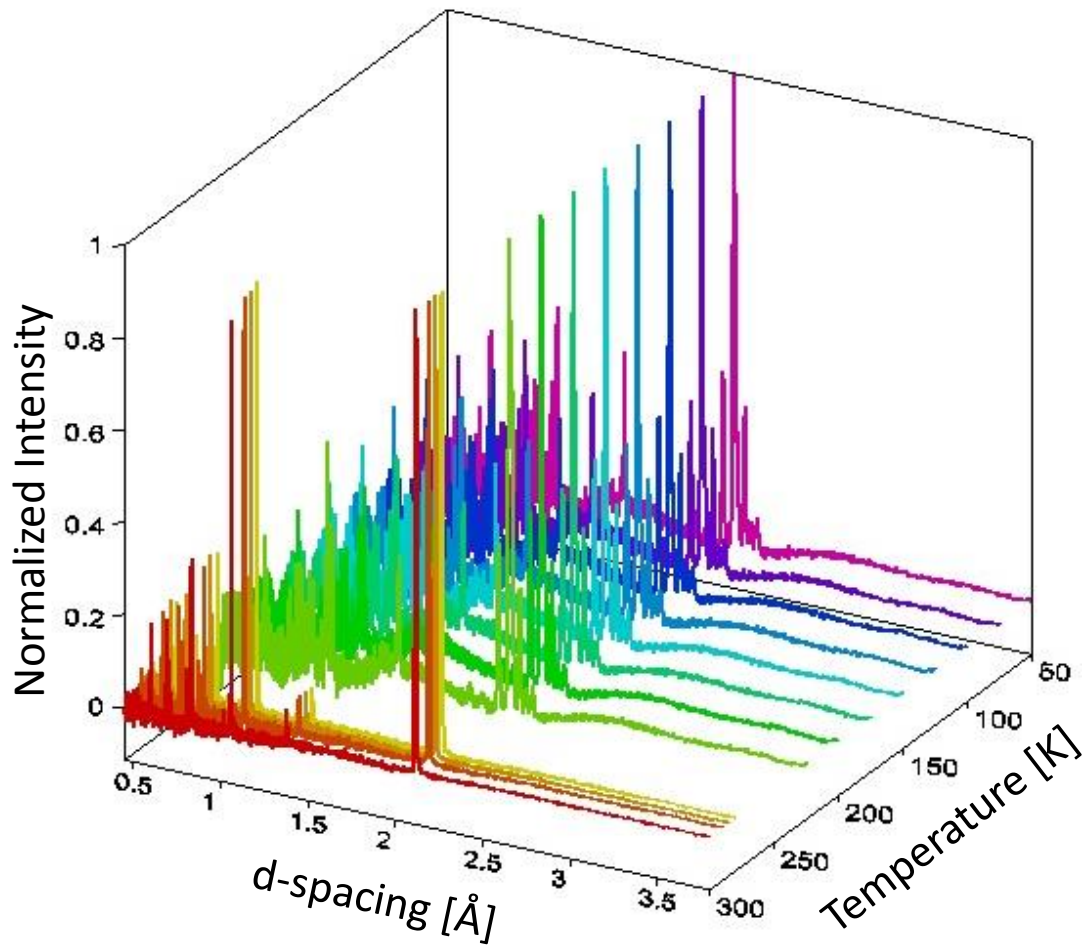
Figure 37. Background subtracted and normalized neutron diffraction data at various temperatures showing cubic austenite at high temperature and modulated martensite at lower temperatures.
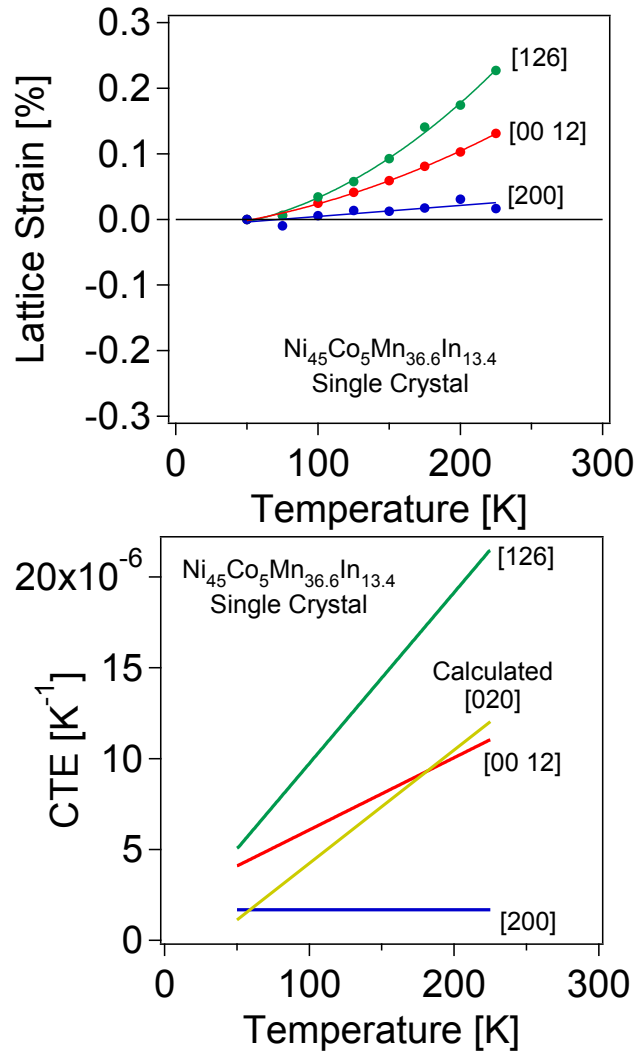
Figure 38. Lattice strain and thermal expansion along different crystallographic directions from neutron diffraction experiments on NiCoMnIn single crystals.

Unfortunately, single crystals were used in the neutron diffractometer which caused systematic peak absences and did not allow complete refinement of the crystal structure. We were not able to calculate the ϵ_{13} term as a result. While this tensor does not show NTE, there is distinct thermal expansion anisotropy. Figure 38b displays CTE values for the various crystallographic directions. Above 200 K, the predicted NTE

directions from the thermodynamic model, [100] and [001], correspond to the low PTE

directions in the material. Below 200 K, the [010] direction's CTE becomes lower than

the [001] direction. While these responses are not fully understood, they are thought to

result from a fundamental change in the entropy difference between the austenite and

martensite at 200 K [65,67]. Below 200 K, the entropy difference between the two phases

becomes smaller.

4.3.4 Tailored Macroscopic Thermal Expansion Via Processing

While the thermal expansion tensors for the alloys discussed are negative in

certain crystallographic directions, they do not produce NTE in bulk materials with

randomly oriented martensite variants. This can easily be seen by estimating the

randomly oriented volume thermal expansion with the trace of the thermal expansion

tensors:

$$NiTiPd: Trace(\epsilon_{ij}) = 36.88 \times 10^{-6} \frac{1}{K}$$

$$CoNiGa: Trace(\epsilon_{ij}) = 15.14 + 0.299T \times 10^{-6} \frac{1}{K}$$

As a result, the martensite variants must be oriented in order to realize tailored

thermal expansion properties in a bulk material. Several processing routes are proposed

to obtain tailored thermal expansion properties in bulk materials, but they all rely on the

fundamental principle of orienting or texturing the martensitic phase. The bulk material

will then have an anisotropic thermal expansion response that is the sum of the various

oriented crystallites. The processing techniques include: 1) rolling, 2) wire drawing, 3)

conventional extrusion, 4) equal channel angular extrusion, 5) precipitation heat

89

treatments under stress, 6) monotonic tension/compression processing and 7) cyclic thermal training under stress (subsequently referred to as SMA training). By applying these processing techniques at various temperatures, one can obtain desired macroscopic thermal expansion characteristics.

Rolling, wire drawing and conventional extrusion are very common techniques for metal forming. They rely on plastic deformation by forcing the material through consecutively smaller gaps which usually result in highly textured materials. For example, a very strong [111] texture can be created by extruding or wire drawing a BCC alloy. While these are conventional techniques, their use to orient martensite variants purely for the purpose of obtaining negative thermal expansion is novel.

Less common techniques that can be used to texture martensite through plastic deformation are equal-channel-angular extrusion and monotonic tension/compression. For equal-channel-angular extrusion, a metal billet is forced through a 90 degree bend which aligns martensite grains. The advantage to this technique is the material's cross-sectional area is not changed after processing. Monotonic tension or compression involves applying tension or compression forces in a single direction to orient martensite variants.

SMA training is a common technique for obtaining stable martensitic transformations and the two way shape memory effect in shape memory alloys. This technique forces an oriented martensite structure to be formed upon transformation, but has never been used for the sole purpose of tailoring a bulk material's thermal expansion properties. The training involves holding a sample under constant load and

heating/cooling across the martensitic transformation temperatures. This forces small amounts of plastic deformation that favor martensite orientation and can produce a tailored thermal expansion.

Precipitation heat treatments are a very common strengthening mechanism in alloy design, but their use for orienting martensite to obtain a tailored thermal expansion material is new. The idea is to load the material and heat it to sufficient temperatures to precipitate small secondary phases that stress the material after cooling. The load would orient the precipitates while they are forming. They will in turn orient martensite with the oriented stresses created during cooling.

4.3.4.1 Cold Rolling

We will now experimentally validate the creation of a tailored thermal expansion via cold rolling. NiTiPd is used as a test system because it is ductile and has high transformation temperatures relative to the other alloys examined. Figure 39a and 38b displays the [111] and [002] pole figures for orthorhombic martensite in the as received material. The extrusion direction (ED) and transverse direction (TD) correspond to the hot extruded directions performed prior to cutting the samples. It is evident that the [111] and [002] planes are not oriented along the extruded direction and are instead along the transvers direction.
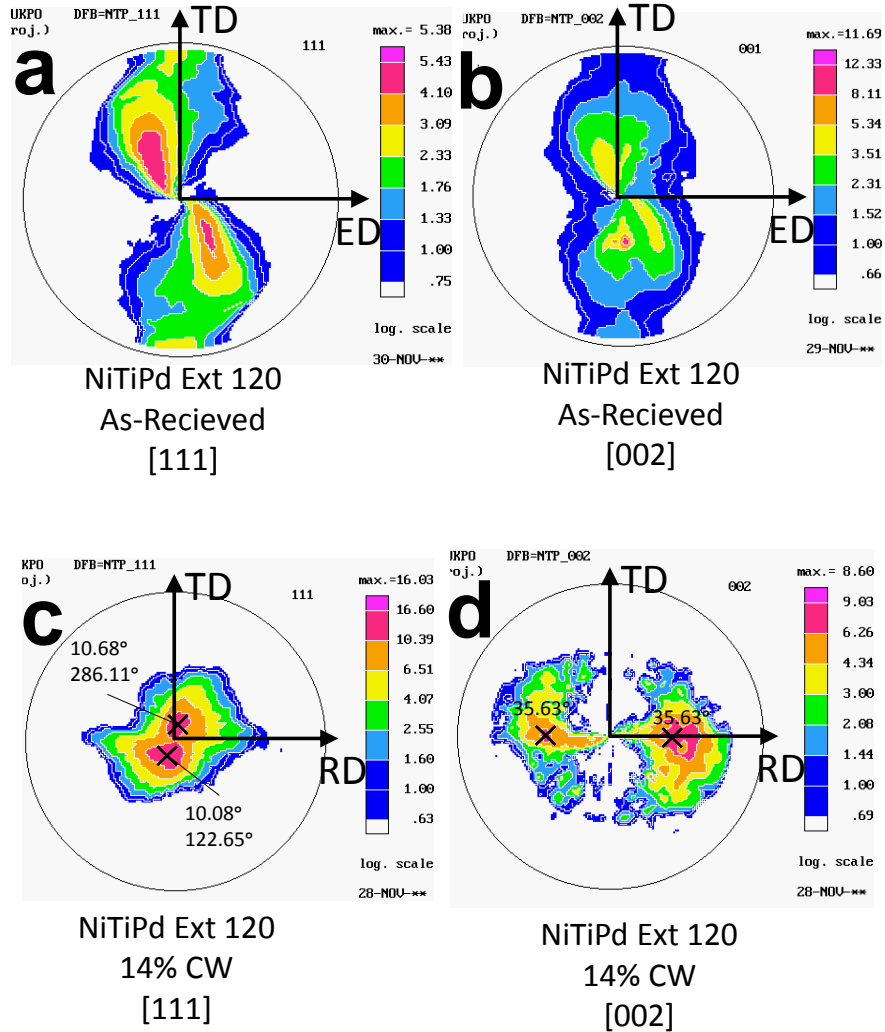
Figure 39. Pole figures for the [111] and [002] orthorhombic planes in martensitic NiTiPd before, a) and b), and after, c) and d), 14% cold working (CW) via rolling at room temperature.

After CR, the sample's texture changes greatly as shown in Figure 39c and 38d. It should be noted that the rolling direction (RD) is in the same direction as the ED for the as-received material. The cold rolling produced significant [111] texturing along the normal direction (ND) while orienting the [002] planes along the RD. A distinct 180º

rotational symmetry along the rolling direction axis is evident and may be a result of the original texture.

Comparison of the thermal expansion is displayed in Figure 40. The initial thermal expansion is 14.9×10^{-6} K^{-1} which changes drastically to 1.99×10^{-6} K^{-1} with only 14% cold work. This is a lower thermal expansion coefficient than super invar at 2.5×10^{-6} K^{-1} in the same temperature range. Interestingly, the thermal expansion properties were isotropic in the rolling plane. This is thought to occur due to the fan-like texture observed for the [002] plane after rolling. The strong [111] texture aligns the PTE direction, [010], mostly in the ND and aligns the NTE directions, [100] and [001], mostly in the RD and TD.
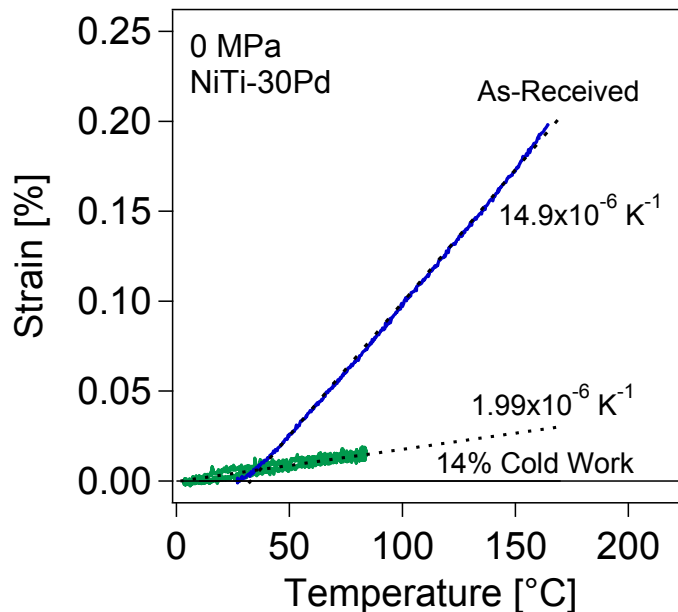
Figure 40. Macroscopic strain vs. temperature and corresponding macroscopic thermal expansion for the as-received and 14% cold worked NiTiPd.

4.3.4.2 Monotonic Tensile Testing

Another mechanism for tailoring the thermal expansion properties is tensile processing. The monotonic tension processing scheme and resulting thermal expansion responses are shown in Figure 41. The sample was heated and cooled under 0 MPa, Figure 41b, after being subjected to the incremental strains shown in Figure 41a. It is easily seen that a tailored thermal expansion coefficient can be obtained by varying the degree of initial strain and a negative thermal expansion can ultimately be reached. It should be noted that this wide range of linear thermal expansion is larger than that of super Invar; which is limited to between 0 ºC and 100 ºC. Figure 41c shows the thermal expansion coefficient vs the maximum induced tensile strain. This shows that the macroscopic thermal expansion coefficient is linearly related to the amount of induced strain and the crossover from positive to negative thermal expansion occurs just above 4% strain.
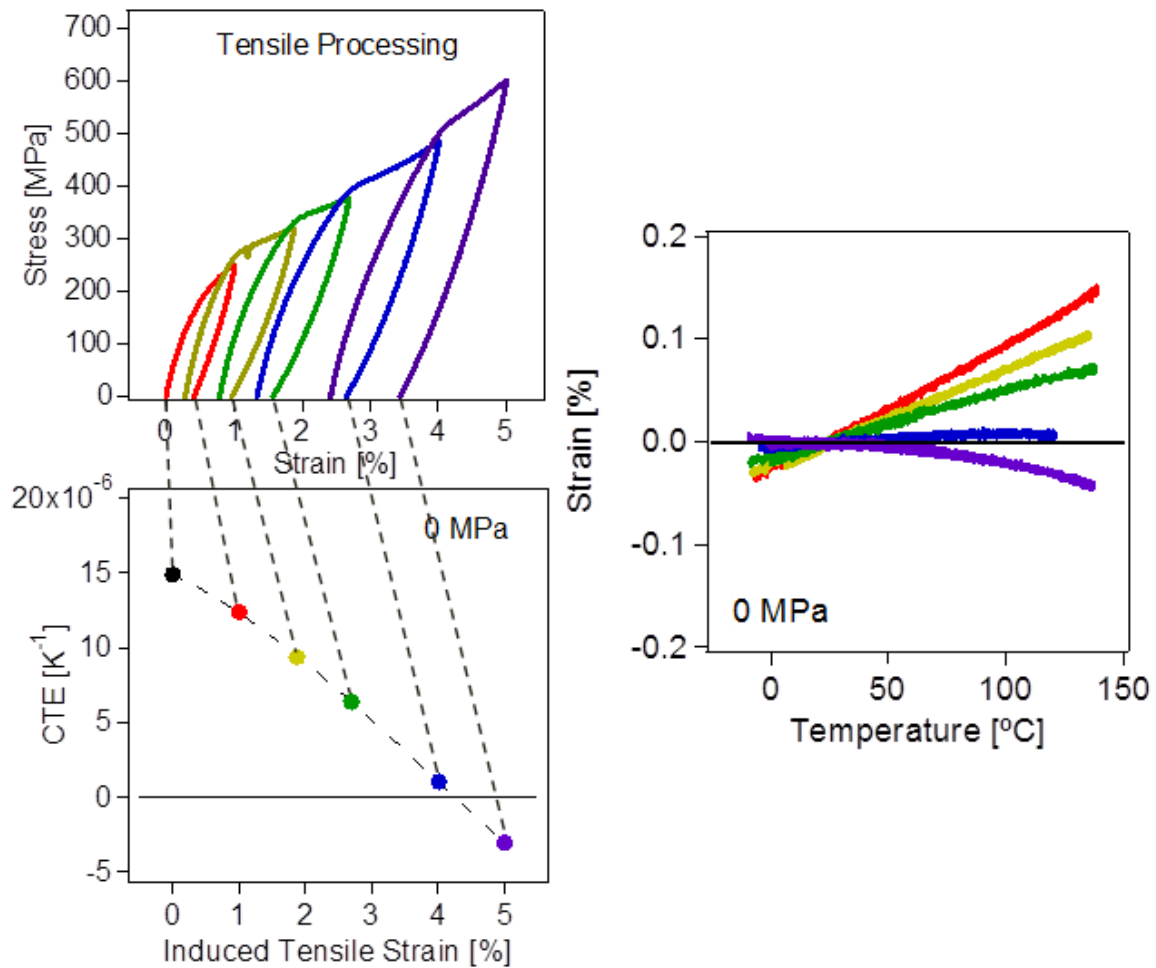
Figure 41. The (a) Stress vs strain for incrementally tensile processed response, (b) 0 MPa heating-cooling response after incremental tensile processing and (c) thermal expansion coefficient vs maximum induced tensile strain for a martensitic NiTiPd alloy.

4.3.4.3 Shape Memory Alloy Training

Other forms of processing include cyclic thermal cycles similar to SMA actuator training. Figure 42 shows a summary of the responses obtained in the NiTiPd test material in the unprocessed, loaded, rolled and SMA trained conditions for comparison with one another. When the material is initially loaded to 200 MPa and taken through a

single SMA cycle (200 MPa Unprocessed condition), the load orients martensite during

the martensitic transformation and a $-4.69 \times 10^{-6} \frac{1}{K}$ NTE is observed. This shows that

martensite variant reorientation is much more effective if the sample is taken through the

martensitic transformation region. It also proves for the first time that NTE can be

sustained under external loads. The sample was then trained for 200 cycles under 200

MPa producing the SMA trained condition. This material exhibits a $-7.3 \times 10^{-6} \frac{1}{K}$ NTE

when tested under 0 MPa which shows the NTE is stable in SMA trained materials even

after the biased load is removed.
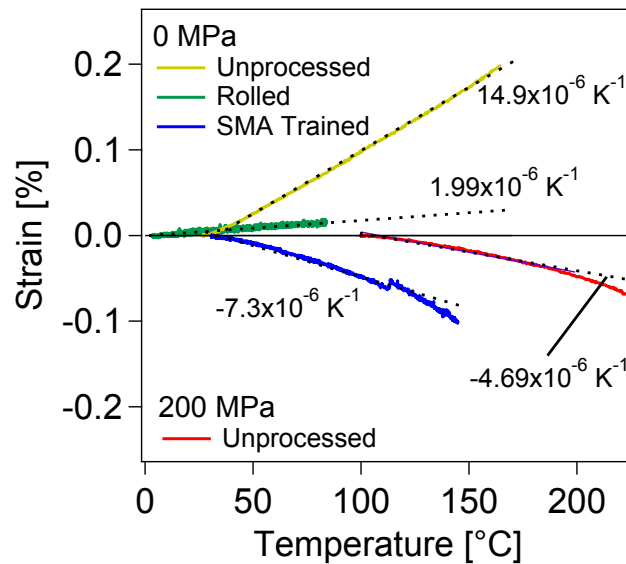
Figure 42. Strain vs temperature for martensitic NiTiPd that shows changes in thermal expansion coefficient under 200 MPa with no processing and under 0 MPa after simple processing.

96

4.4 Conclusions

In conclusion, a statistical thermodynamic model was proposed to explain the large positive and negative thermal expansion observed NiTi and alpha uranium. The thermal expansion directions were successfully predicted for a variety of shape memory alloys with different martensitic structures. The predictive capabilities combined with knowledge of the underlying mechanism can potentially allow identification of many other alloy systems that will show large thermal expansion anisotropy. The thermal expansion anisotropy is also useful for creating bulk materials with tailored thermal expansion coefficients. Several processing routes were chosen for demonstration, but any processing route that orients martensite variants can potentially create tailored thermal properties. Future work will focus on verifying the statistical thermodynamic model through neutron diffraction experiments, identifying additional alloy systems that will show thermal expansion anisotropy and exploring processing routes for obtaining tailored thermal expansion in bulk materials.

CHAPTER V

CONCLUSIONS

In conclusion, this pioneering work has explored several new application possibilities for shape memory alloys. The first meta-magnetic shape memory alloy foams with shape memory properties were created for use a magnetically morphing tissue scaffolds. While they ultimately do not show promise for in vivo biomedical applications due to their cytotoxicity, the improved corrosion resistance from polymer passivation coatings, greater fracture resistance and higher heat transfer coefficients make these alloy foams excellent candidates magneto and elasto caloric applications. Two types of glassy relaxation, strain and super spin, were directly observed in a single alloy composition with simple secondary heat treatments. While we only explored the existence and stabilization of these glasses, they provide new application possibilities such as magnetic sensing for data storage and shape memory actuators with a perfect one way shape memory response. Finally, we explored the thermal expansion anisotropy in a host of shape memory alloy systems. We were able to predict the thermal expansion directions with a statistical thermodynamic model and ultimately process these alloys to tailor the bulk thermal expansion properties. These tailored thermal expansion properties in alloys are unprecedented in their large temperature window and linearity. This will provide engineers in all disciplines with a design tool previously unavailable and its impact will be wide reaching.

REFERENCES

1   Ito, K. *et al.* Mechanical and shape memory properties of Ni43Co7Mn39Sn11 alloy compacts fabricated by pressureless sintering. *Scripta Materialia* **63**, 1236-1239, (2010).

2   Ito, K. *et al.* Martensitic transformation in NiCoMnSn metamagnetic shape memory alloy powders. *Materials Transactions* **49**, 1915-1918, (2008).

3   Chmielus, M., Zhang, X. X., Witherspoon, C., Dunand, D. C. & Mullner, P. Giant magnetic-field-induced strains in polycrystalline Ni-Mn-Ga foams. *Nat Mater* **8**, 863-866, (2009).

4   Acet, M. Magnetic shape memory: Magnetoelastic sponges. *Nat Mater* **8**, 854-855, (2009).

5   Wang, G. *et al.* Study on powder metallurgical preparation of NiCoMnIn alloy foam. *Materials Science Forum* **654-656**, 1331-1334, (2010).

6   Wang, Y., Ren, X., Otsuka, K. & Saxena, A. Temperature-stress phase diagram of strain glass Ti48.5Ni51.5. *Acta Materialia* **56**, 2885-2896, (2008).

7   Ito, W. *et al.* Kinetic arrest of martensitic transformation in the NiCoMnIn metamagnetic shape memory alloy. *Applied Physics Letters* **92**, (2008).

8   Bhatti, K. P., El-Khatib, S., Srivastava, V., James, R. D. & Leighton, C. Small-angle neutron scattering study of magnetic ordering and inhomogeneity across the martensitic phase transformation in Ni50-xCoxMn40Sn10 alloys. *Physical Review B* **85**, (2012).

9   Qiu, S. *et al.* Measurement of the lattice plane strain and phase fraction evolution during heating and cooling in shape memory NiTi. *Applied Physics Letters* **95**, (2009).

10   Monroe, J. A. *et al.* Determining recoverable and irrecoverable contributions to accumulated strain in a NiTiPd high-temperature shape memory alloy during thermomechanical cycling. *Scripta Materialia* **65**, 123-126, (2011).

11   Mauney, J. R. *et al.* Mechanical stimulation promotes osteogenic differentiation of human bone marrow stromal cells on 3-D partially demineralized bone scaffolds in vitro. *Calcified Tissue International* **74**, 458-468, (2004).

12   Doroski, D. M., Levenston, M. E. & Temenoff, J. S. Cyclic tensile culture promotes fibroblastic differentiation of marrow stromal cells encapsulated in

poly(ethylene glycol)-based hydrogels. *Tissue Engineering Part A* **16**, 3457-3466, (2010).

13   Chmielus, M., Zhang, X. X., Witherspoon, C., Dunand, D. C. & Muellner, P. Giant magnetic-field-induced strains in polycrystalline Ni-Mn-Ga foams. *Nature Materials* **8**, 863-866, (2009).

14   Acet, M. Magnetic shape memory magnetoelastic sponges. *Nature Materials* **8**, 854-855, (2009).

15   Sozinov, A., Likhachev, A. A., Lanska, N. & Ullakko, K. Giant magnetic-field-induced strain in NiMnGa seven-layered martensitic phase. *Applied Physics Letters* **80**, 1746-1748, (2002).

16   Sasso, C. P., Zheng, P., Basso, V., Muellner, P. & Dunand, D. C. Enhanced field induced martensitic phase transition and magnetocaloric effect in Ni55Mn20Ga25 metallic foams. *Intermetallics* **19**, 952-956, (2011).

17   Karaca, H. E. *et al.* Magnetic field-induced phase transformation in NiMnColn magnetic shape-memory alloys-a new actuation mechanism with large work output. *Advanced Functional Materials* **19**, 983-998, (2009).

18   Ito, K. *et al.* Metamagnetic shape memory effect in polycrystalline NiCoMnSn alloy fabricated by spark plasma sintering. *Scripta Materialia* **61**, 504-507, (2009).

19   Wang, G. *et al.* in *Pricm 7, Pts 1-3* Vol. 654-656 *Materials Science Forum* (eds J. F. Nie & A. Morton) 1331-1334 (2010).

20   Chatterjee, S., Giri, S., De, S. K. & Majumdar, S. in *Ferromagnetic Shape Memory Alloys* Vol. 52 *Advanced Materials Research* (ed L. Manosa) 215-220 (2008).

21   Pouponneau, P. *et al. Biocompatibility of candidate materials for the realization of medical microdevices.* (2006).

22   Hartwig, A., Kruger, I. & Beyersmann, D. Mechanisms in nicke genotoxicity - the significance of interactions with DNA-repair. *Toxicology Letters* **72**, 353-358, (1994).

23   Laing, P. G., Ferguson, A. B. & Hodge, E. S. Tissue reaction in rabbit muscle exposed to metallic implants. *J Biomed Mat Res* **1**, 135-149, (1967).

24   Pulido, M. D. & Parrish, A. R. Metal-induced apoptosis: mechanisms. *Mutation Research-Fundamental and Molecular Mechanisms of Mutagenesis* **533**, 227-241, (2003).

25   Putters, J. L. M., Sukul, D., Dezeeuw, G. R., Bijma, A. & Besselink, P. A. Comparative cell-culture effects of shape memory metal (Nitinol (R)), nickel and titanium - a biocompatibility estimation. *European Surgical Research* **24**, 378-382, (1992).

26   Sullivan, M. R. *et al.* In situ study of temperature dependent magnetothermoelastic correlated behavior in ferromagnetic shape memory alloys. *Journal of Applied Physics* **95**, 6951-6953, (2004).

27   Crossgrove, J. & Zheng, W. Manganese toxicity upon overexposure. *Nmr in Biomedicine* **17**, 544-553, (2004).

28   Keen, C. L., Ensunsa, J. L. & Clegg, M. S. in *Metal Ions in Biological Systems; Manganese and its role in biological processes* Vol. 37 *Metal Ions in Biological Systems* 89-121 (2000).

29   Yamamoto, A., Honma, R. & Sumita, M. Cytotoxicity evaluation of 43 metal salts using murine fibroblasts and osteoblastic cells. *Journal of Biomedical Materials Research* **39**, 331-340, (1998).

30   Dai, J. H., Sullivan, D. M. & Bruening, M. L. Ultrathin, layered polyamide and polyimide coatings on aluminum. *Industrial & Engineering Chemistry Research* **39**, 3528-3535, (2000).

31   Hoffmann, K., Friedrich, T. & Tieke, B. Layer-by-layer assembled polyelectrolyte blend membranes and their use for ion separation and rejection. *Polymer Engineering and Science* **51**, 1497-1506, (2011).

32   Lackmann, J. *et al.* Formability of thermally cured and of nanoclay-reinforced polyelectrolyte films on NiTi substrates. *Journal of Materials Science* **47**, 151-161, (2012).

33   Lackmann, J., Regenspurger, R., Maxisch, M., Grundmeier, G. & Maier, H. J. Defect formation in thin polyelectrolyte films on polycrystalline NiTi substrates. *Journal of the Mechanical Behavior of Biomedical Materials* **3**, 436-445, (2010).

34   Ito, W. *et al.* Concentration dependence of magnetic moment in Ni50-xCoxMn50-yZy, (Z=In,Sn) Heusler alloys. *Applied Physics Letters* **97**, (2010).

35   Wang, X., Li, Y., Xiong, J., Hodgson, P. D. & Wen, C. e. Porous TiNbZr alloy scaffolds for biomedical applications. *Acta Biomaterialia* **5**, 3616-3624, (2009).

36   Bogdanski, D. *et al.* Easy assessment of the biocompatibility of Ni-Ti alloys by in vitro cell culture experiments on a functionally graded Ni-NiTi-Ti material. *Biomaterials* **23**, 4549-4555, (2002).

37   Bryant, S. J., Nuttelman, C. R. & Anseth, K. S. Cytocompatibility of UV and visible light photoinitiating systems on cultured NIH/3T3 fibroblasts in vitro. *Journal of Biomaterials Science-Polymer Edition* **11**, 439-457, (2000).

38   Cui, Z. D. *et al.* Improving the biocompatibility of NiTi alloy by chemical treatments: An in vitro evaluation in 3T3 human fibroblast cell. *Materials Science & Engineering C-Biomimetic and Supramolecular Systems* **28**, 1117-1122, (2008).

39   El Medawar, L. *et al.* Electrochemical and cytocompatibility assessment of NiTiNOL memory shape alloy for orthodontic use. *Biomolecular Engineering* **19**, 153-160, (2002).

40   Harris, J. J., DeRose, P. M. & Bruening, M. L. Synthesis of passivating, nylon-like coatings through cross-linking of ultrathin polyelectrolyte films. *Journal of the American Chemical Society* **121**, 1978-1979, (1999).

41   Warren, B. E. & Biscoe, J. Fourier analysis of X-ray patterns of soda-silica glass. *Journal of the American Ceramic Society* **21**, 259-265, (1938).

42   Wang, Y. *et al.* Evidence for ferromagnetic strain glass in Ni-Co-Mn-Ga Heusler alloy system. *Applied Physics Letters* **101**, (2012).

43   Wang, Y., Ren, X., Otsuka, K. & Saxena, A. Evidence for broken ergodicity in strain glass. *Physical Review B* **76**, (2007).

44   Zhang, J. *et al.* Spontaneous strain glass to martensite transition in a Ti50Ni44.5Fe5.5 strain glass. *Physical Review B* **84**, (2011).

45   Zhou, Y. M. *et al.* High temperature strain glass in Ti-50(Pd50-xCrx) alloy and the associated shape memory effect and superelasticity. *Applied Physics Letters* **95**, (2009).

46   Zhou, Y. M. *et al.* Strain glass in doped Ti-50(Ni50-xDx) (D = Co, Cr, Mn) alloys: Implication for the generality of strain glass in defect-containing ferroelastic systems. *Acta Materialia* **58**, 5433-5442, (2010).

47   Ren, X. B. *et al.* Ferroelastic nanostructures and nanoscale transitions: ferroics with point defects. *Mrs Bulletin* **34**, 838-846, (2009).

48   Wang, Y. *et al.* Evidence for ferromagnetic strain glass in Ni-Co-Mn-Ga Heusler alloy system. *Applied Physics Letters* **101**, 101913, (2012).

49   Wang, D. P. *et al.* Transition in superelasticity for Ni55-xCoxFe18Ga27 alloys due to strain glass transition. *Epl* **98**, (2012).

50   Sharma, V. K. *et al.* The effect of substitution of Mn by Fe and Cr on the martensitic transition in the Ni50Mn34In16 alloy. *Journal of Physics-Condensed Matter* **22**, (2010).

51   Kumar, K. *et al.* Relating supercooling and glass-like arrest of kinetics for phase separated systems: Doped CeFe_{2} and (La,Pr,Ca)MnO_{3}. *Physical Review B* **73**, 184435, (2006).

52   Binder, K. & Young, A. P. Spin-glasses - experimental facts, theoretical concepts, and open questions. *Reviews of Modern Physics* **58**, 801-976, (1986).

53   Edwards, S. F. & Anderson, P. W. Theory of spin glasses. *Journal of Physics F-Metal Physics* **5**, 965-974, (1975).

54   Cong, D. Y., Roth, S. & Schultz, L. Magnetic properties and structural transformations in Ni-Co-Mn-Sn multifunctional alloys. *Acta Materialia* **60**, 5335-5351, (2012).

55   Roy, S. B. *et al.* Evidence of a magnetic glass state in the magnetocaloric material Gd_{5}Ge_{4}. *Physical Review B* **74**, 012403, (2006).

56   Prado, M. O., Lovey, F. C. & Civale, L. Magnetic properties of Cu–Mn–Al alloys with shape memory effect. *Acta Materialia* **46**, 137-147, (1998).

57   Yoo, P.-K. *et al.* Spin glass behaviour of Cu--Zn--Al--Mn shape memory alloy. *Journal of Materials Science Letters* **17**, 173-175, (1998).

58   Cahn, R. W. Materials science - multiple Kauzmann paradoxes. *Nature* **373**, 475-476, (1995).

59   Stillinger, F. H., Debenedetti, P. G. & Truskett, T. M. The Kauzmann paradox revisited. *Journal of Physical Chemistry B* **105**, 11809-11816, (2001).

60   Kishore, K. & Shobha, H. K. Entropy catastrophe and configurational entropies in supercooled and superheated regimes. *Journal of Chemical Physics* **101**, 7037-7047, (1994).

61   Ito, W. *et al.* Atomic ordering and magnetic properties in the Ni[sub 45]Co[sub 5]Mn[sub 36.7]In[sub 13.3] metamagnetic shape memory alloy. *Applied Physics Letters* **93**, 232503, (2008).

62   Ito, W., Umetsu, R. Y., Kainuma, R., Kakeshita, T. & Ishida, K. Heat-induced and isothermal martensitic transformations from kinetically arrested parent phase in NiCoMnIn metamagnetic shape memory alloy. *Scripta Materialia* **63**, 73-76, (2010).

63   Karaca, H. E. *et al.* Shape memory and pseudoelasticity response of NiMnCoIn magnetic shape memory alloy single crystals. *Scripta Materialia* **58**, 815-818, (2008).

64   Lee, Y. H. *et al.* Isothermal nature of martensitic transformation in an Ni45Co5Mn36.5In13.5 magnetic shape memory alloy. *Scripta Materialia* **64**, 927-930, (2011).

65   Monroe, J. A. *et al.* Direct measurement of large reversible magnetic-field-induced strain in Ni-Co-Mn-In metamagnetic shape memory alloys. *Acta Materialia* **60**, 6883-6891, (2012).

66   Xu, X., Ito, W., Katakura, I., Tokunaga, M. & Kainuma, R. In situ optical microscopic observation of NiCoMnIn metamagnetic shape memory alloy under pulsed high magnetic field. *Scripta Materialia* **65**, 946-949, (2011).

67   Xu, X., Ito, W., Umetsu, R. Y., Kainuma, R. & Ishida, K. Anomaly of critical stress in stress-induced transformation of NiCoMnIn metamagnetic shape memory alloy. *Applied Physics Letters* **95**, (2009).

68   Krenke, T. *et al.* Ferromagnetism in the austenitic and martensitic states of Ni-Mn-In alloys. *Physical Review B* **73**, 174413, (2006).

69   Ishikawa, H. *et al.* Atomic ordering and magnetic properties in Ni2Mn(GaxAl1-x) Heusler alloys. *Acta Materialia* **56**, 4789-4797, (2008).

70   Cross, L. E. Relaxor ferroelectrics. *Ferroelectrics* **76**, 241-267, (1987).

71   Umetsu, R. Y. *et al.* Kinetic arrest behavior in martensitic transformation of NiCoMnSn metamagnetic shape memory alloy. *Journal of Alloys and Compounds* **509**, 1389-1393, (2011).

72   Karaca, H. E. *et al.* On the stress-assisted magnetic-field-induced phase transformation in Ni2MnGa ferromagnetic shape memory alloys. *Acta Materialia* **55**, 4253-4269, (2007).

73   Wang, Y. *et al.* Evolution of the relaxation spectrum during the strain glass transition of Ti48.5Ni51.5 alloy. *Acta Materialia* **58**, 4723-4729, (2010).

74   Sasioglu, E., Sandratskii, L. M. & Bruno, P. Role of conduction electrons in mediating exchange interactions in Mn-based Heusler alloys. *Physical Review B* **77**, (2008).

75   Ruderman, M. A. & Kittel, C. Indirect exchange coupling of nuclear magnetic moments by conduction electrons. *Physical Review* **96**, 99-102, (1954).

76   Graf, T., Felser, C. & Parkin, S. S. P. Simple rules for the understanding of Heusler compounds. *Progress in Solid State Chemistry* **39**, 1-50, (2011).

77   Pati, S. R. & Cohen, M. Nucleation of isothermal martensitic transformation. *Acta Metallurgica* **17**, 189-&, (1969).

78   Kustov, S., Corro, M. L., Pons, J. & Cesari, E. Entropy change and effect of magnetic field on martensitic transformation in a metamagnetic Ni-Co-Mn-In shape memory alloy. *Applied Physics Letters* **94**, (2009).

79   Takenaka, K. Negative thermal expansion materials: technological key for control of thermal expansion. *Science and Technology of Advanced Materials* **13**, (2012).

80   Lloyd, L. T. & Barrett, C. S. Thermal expansion of alpha uranium. *Journal of Nuclear Materials* **18**, 55-&, (1966).

81   McMahon, M. I. & Nelmes, R. J. High-pressure structures and phase transformations in elemental metals. *Chemical Society Reviews* **35**, 943-963, (2006).

82   Niinomi, M., Nakai, M., Akahori, T. & Tsutsumi, H. in *Thermec 2009, Pts 1-4* Vol. 638-642 *Materials Science Forum* (eds T. Chandra, N. Wanderka, W. Reimers, & M. Ionescu) 16-21 (2010).

83   Liu, Z.-K., Wang, Y. & Shang, S.-L. Origin of negative thermal expansion phenomenon in solids. *Scripta Materialia* **65**, 664-667, (2011).

84   Jacob, C. W. & Warren, B. E. The crystalline structure of uranium. *Journal of the American Chemical Society* **59**, 2588-2591, (1937).